J Therm Spray Tech (2021) 30:617–642
https://doi.org/10.1007/s11666-020-01110-w

PEER REVIEWED

Influence of MAX-Phase Deformability on Coating Formation by Cold Spraying

Andreas Elsenberg[1] · Marco Busato[1,2] · Frank Gärtner[1] · Alexander List[1] · Alessia Bruera[1,2] · Giovanni Bolelli[2,3,4] · Luca Lusvarghi[2,3,4] · Thomas Klassen[1]

Submitted: 3 July 2020 / in revised form: 2 October 2020 / Accepted: 6 October 2020 / Published online: 8 November 2020

Abstract As solid-state deposition technique avoiding oxidation, cold gas spraying is capable of retaining feedstock material properties in the coatings, but typically fails to build up coatings of brittle materials. Ceramic MAX phases show partial deformability in particular lattice directions and may thus successfully deposit in cold spraying. However, deformation mechanisms under high strain rate, as necessary for cohesion and adhesion, are not fully clear yet. A MAX-phase deposit only builds up, if the specific mechanical properties of the MAX phase allow for, and if suitable spray parameter sets get realized. To investigate the influence of material properties and deposition conditions on coating microstructure and quality, three MAX phases, Ti_3SiC_2, Ti_2AlC and Cr_2AlC, were selected. Up to ten passes under different spray parameters yielded Ti_2AlC and Cr_2AlC coatings with thicknesses of about 200-500 µm. In contrast, Ti_3SiC_2 only forms a monolayer, exhibiting brittle laminar failure of the impacting particles. In all cases, the crystallographic structure of the MAX-phase powders was retained in the coatings. Thicker coatings show rather low porosities (< 2%), but some laminar cracks. The deposition behavior is correlated with individual mechanical properties of the different MAX-phase compositions and is discussed regarding the particular, highly anisotropic deformation mechanisms.

Keywords cold spraying · deformation mechanisms · MAX phases

This article is part of a special topical focus in the Journal of Thermal Spray Technology on Aerosol Deposition and Kinetic Spray Processes. This issue was organized by Dr. Kentaro Shinoda, National Institute of Advanced Industrial Science and Technology (AIST); Dr. Frank Gaertner, Helmut-Schmidt University; Prof. Changhee Lee, Hanyang University; Prof. Ali Dolatabadi, Concordia University; and Dr. Scooter Johnson, Naval Research Laboratory.

✉ Andreas Elsenberg
Andreas.Elsenberg@hsu-hh.de

[1] Helmut-Schmidt-University/University of the Federal Armed Forces, Holstenhofweg 85, 22043 Hamburg, Germany

[2] Dipartimento di Ingegneria "Enzo Ferrari", Università di Modena e Reggio Emilia, Via Pietro Vivarelli 10/1, 41125 Modena, MO, Italy

[3] InterMech – MO.RE. Centro Interdipartimentale per la Ricerca Applicata e i Servizi nel Settore della Meccanica Avanzata e della Motoristica, Università di Modena e Reggio Emilia, Via Pietro Vivarelli 2, 41125 Modena, MO, Italy

[4] Consorzio Interuniversitario Nazionale per la Scienza e Tecnologia dei Materiali (INSTM), Local Unit: Università di Modena e Reggio Emilia, Via Pietro Vivarelli 10/1, 41125 Modena, MO, Italy

Introduction

MAX phases attract increasing attention with respect to possible applications due to their unique property combination of covalently bonded ceramics and metals in one crystal structure (Ref 1). The crystallographic structure of the MAX phases with atomic metal layers stacked in between covalent ceramics enables electrical conductivity and a good machinability (Ref 2, 3). The mechanical deformation of MAX phases is mainly attributed to the role of the metal layer and locally weaker bonds and associated dislocation gliding mechanisms in the basal plane, or kink banding often causing internal delamination (Ref 1, 4-7). The general formula $M_{n+1}AX_n$ describes the composition with M as an early transition metal (Ti, Zr, Cr…), A as an IIIA-group element (Si, Al…) and X as carbon or nitrogen (Ref 8). By their high melting temperature and the ability

to form a stable oxide scale on the surface (Ref 9), a number of MAX-phase materials have a high potential to serve as protective layer in high-temperature applications up to temperatures of more than 1200 °C (Ref 10). Al- or Cr-based MAX phases especially show a good resistance to oxidation (Ref 11, 12). As bulk materials, MAX phases are usually synthesized by thermal reaction from the different elemental powders (Ref 12).

Processing of MAX-phase coatings is most prominently performed by physical vapor deposition (PVD) (Ref 13, 14), resulting in thin films with a layer thickness usually lower than 5 µm (Ref 15). Thicker coatings can be deposited by thermal spraying such as high-velocity oxygen-fuel (HVOF) (Ref 16-20), high-velocity air–fuel (HVAF) (Ref 20) or atmospheric plasma spraying (APS) (Ref 19), using milled powder as feedstock. Thermally sprayed MAX phases can be processed to low-porosity coatings showing a good adhesion to the substrate. Internal delamination at particle–particle interfaces and cracks are only obtained after hardness testing. However, due to melting during the thermal spray process and the exposure to environmental oxygen, the phase content of coatings typically differs from that of the feedstock powder because of oxidation and decomposition phenomena. The newly formed phases, such as oxides, simpler non-MAX carbides and intermetallics, reduce the coating performance in high-temperature applications as compared to bulk MAX phases of similar compositions.

In contrast to thermal spraying, cold spraying (CS) or kinetic spraying operates with powder impacts in the solid state and thus avoids oxidation and undesired phase formation by solidification from the liquid state. Cold spraying has been mainly applied to ductile metals, which under high strain-rate deformation during the high-velocity impact bond to the substrate or previously deposited coating layers by adiabatic shear instabilities (ASI) at the interfaces (Ref 21). So far, cold spraying of brittle ceramics mainly resulted in the build-up of a monolayer embedded in the deformed substrate surface showing the needed plastic deformation (Ref 22). Up to now, only few researches describe cold spraying of MAX phases: The examples of Ti_2AlC (Ref 23, 24) and Cr_2AlC (Ref 25) demonstrate that original crystal structures are retained during deposition. However, due to the mainly brittle character of the MAX-phase material, attained deposition efficiencies are rather low (< 20%), and respective coatings show high amounts of internal, mainly lamellar cracks. In an alternative approach, still applying a kinetic spray technique, thin, low-porosity coatings of Ti_3SiC_2 were processed by aerosol deposition (AD) (Ref 26, 27). A comparison of kinetically sprayed coatings of different MAX-phase materials applying the same spray technique and similar parameter sets is so far still missing.

Depending on constituents, atomic composition and thus local structure and bonding, the compressive strength of different MAX-phase materials varies from about 380 to 1900 MPa (Ref 28), the strain to failure being typically less than 10% (Ref 5). The strength of most MAX-phase materials decreases only slightly with increasing temperature over a rather wide range (Ref 29). Thermal softening usually occurs above a material specific softening temperature of about 600 to 800 °C (Ref 29). Missing deformability, i.e., low strain to failure and low thermal softening, is a major obstacle to a possible deposition by cold spraying. Bonding at particle–particle interfaces needs the heat creation by deformation and sufficiently efficient thermal softening to compensate strain and strain hardening effects. Thus, bonding should preferentially occur at particle impact temperatures reaching or exceeding the softening temperature. Modern high-pressure cold spray equipment operates at process gas temperatures of up to 1100 °C. Therefore, despite the cooling by the expanding gas in the divergent section of the de Laval nozzle and the free jet, rather high particle impact temperatures of 600 to 800 °C can be attained, if the spray particles have a sufficiently high thermal inertia (Ref 11, 12). Another obstacle can be given by strain-rate hardening. The few reports on high strain-rate deformation of MAX phases differ greatly, indicating only minor influences for Ti_2AlC (Ref 5) and high strain-rate sensitivity for Ti_3SiC_2 (Ref 30). Strong strain and strain-rate hardening effects counteract thermal softening and might impede the formation of adiabatic shear instabilities (ASI) and thus bonding. In addition, brittle behavior could cause fracture of impacting particles and already deposited layers.

Because of their mechanical bulk properties, Ti_3SiC_2, Ti_2AlC and Cr_2AlC are used as model systems for investigating the features of rather different MAX-phase materials to study impact phenomena and possible coating formation in high-pressure cold spraying. For distinguishing between primary impact and possible fracture by following particles, special emphasis is put on single impact morphologies and the build-up of the first few particle layers. Full coating microstructure and hardness should reveal information on coating integrity with respect to bonded and non-bonded interfaces as well as possible defects as pores and cracks. The study should allow to assess the suitability of different MAX phases for building up coatings by cold spraying.

Conventional interpretations for cold spraying of metals will fail to describe deformation and bonding phenomena of MAX phases, as well as surface damage on substrates or already deposited layers. Thus, this study step by step explores a number of different features to distinguish individual roles of thermal softening on deformation as well as effective particle momentum, to get a better

understanding on the complex interplay between the different phenomena, and also possibly associated surface damage. With that also guidelines should be provided on the role individual particle sizes.

This study is a part of the EU project "IL TROVATORE" that will reduce the risk of fatal meltdowns in the event of a cooling water failure to prevent reactor accidents like in Fukushima in March 2011. The aim is to develop an oxidation protection coating for the Zircaloy fuel rods and to get more time to restore the cooling water circulation. Thus, analyses of hot gas and steam corrosion are still under investigation and will be subject of following publications.

Materials and Experimental Procedures

Materials

The Ti_3SiC_2, Ti_2AlC and Cr_2AlC powders were produced by Sandvik, Sweden, and by milling procedures crushed to sprayable powder sizes. The micrographs in Fig. 1 show overviews (left) and details (right) of the powder morphologies of the Ti_3SiC_2, Ti_2AlC and Cr_2AlC feedstock powders. The morphologies of all three powders are angular, due to production by milling from bulk material. Mean sizes differ by milling conditions and applied classifying procedures. The Ti_3SiC_2 powder was specially manufactured and adapted for the use in cold spraying. The size distribution of the presented Ti_3SiC_2 powder is rather homogenous, since air sifting efficiently removed particles smaller than 25 µm. In contrast, without applying any classifying procedure, the Ti_2AlC and Cr_2AlC powders contain rather high amounts of fine particles or fragments. From the micrographs, it might be judged that the Ti_3SiC_2 particles contain less cracks and are less flattened than the Ti_2AlC and Cr_2AlC particles. Before cold spraying, the powders were dried for 12 h in vacuum to remove possible humidity and enable more stable powder feeding.

Stainless steel AISI 304 and copper plates with a thickness of 3 mm were used as substrates (lateral size 50 × 70 mm for coating production and 50 × 20 mm for performing wipe tests). The surface of the substrates for coating production was used in the as-received state. The substrates for processing the wipe tests were surface polished to a maximum roughness of $R_a \leq 1$ µm. All substrates were cleaned with ethanol before spraying.

Particle Size Analysis

The particle size distributions were measured by laser scattering using an instrument type LA-910 from Horiba, Kyoto, Japan. Details on the particle sizes are given in Table 1. The powder size distributions differ significantly. For Ti_3SiC_2, the rather narrow and coarse distribution is attributed to the classifying procedure. The small sizes of the Ti_2AlC and Cr_2AlC powders and their wide size distribution are due to the high-energy input in the planetary mill and direct use after milling without any classifying. The smaller sizes of the Cr_2AlC powder as compared to those of Ti_2AlC could be attributed to lower fracture strength.

Calculation of Impact Conditions

The impact conditions with respect to particle velocity and particle temperature under the different spray parameter sets were calculated by using the KSS software (Kinetic Spray Solutions GmbH, Buchholz, Germany). The software was also used to supply a first approximation of critical velocities for coating formation by using the algorithm for metallic materials. Needed input data on material properties are taken from the literature for the respective bulk materials and are given in Table 2 (Ref 28, 29, 31). For MAX-phase materials, that shows decomposition before melting, melting temperatures were calculated by GTT-Technologies, Herzogenrath, Germany.

Cold Spraying

Cold spraying was performed with an Impact 5/11 spraying system from Impact Innovations, Rattenkirchen, Germany. Nitrogen was used as carrier and process gas. For studying influences from process conditions on coating formation, parameters as the gas pressure and the gas temperature were varied in ranges from 40 to 50 bar and from 800 to 1100 °C, respectively. In addition, also the line traverse speed was varied in a range from 100 to 500 mm/s and the powder feed rate was kept fixed at 4.3 cm^3/min. For processing wipe test samples, a high traverse speed of 1000 mm/s was used at minimum powder feed rates of 0.43 cm^3/min. The stand-off distance and the distance between spray lines were kept fixed at 60 and 2 mm, respectively. Individual details on the spray parameters used for the different MAX-phase material are given in Table 3. The deposition efficiencies (DE) were determined as the ratios between the rates of mass gain of coated substrates and the applied powder feed rates.

Microscopy

The microstructures of the coatings were analyzed by digital optical microscopy (OM) using a VHX-S660E from Keyence Ōsaka, Japan, and by scanning electron microscopy (SEM) using a Nova NanoSEM 450 from FEI-ThermoFisher Scientific (Waltham, Massachusetts, USA)

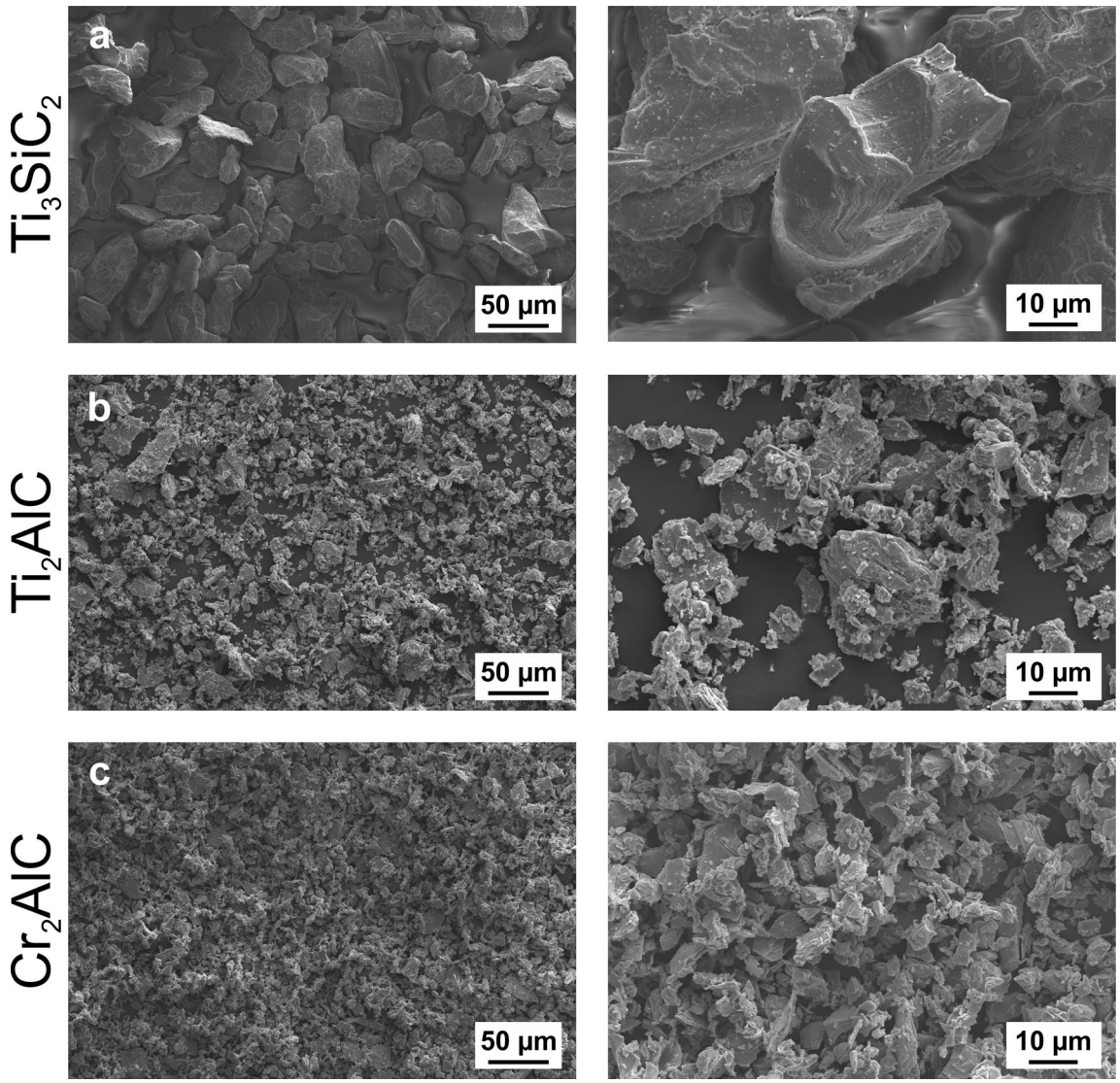

Fig. 1 SEM micrographs showing the morphologies of the (a) Ti_3SiC_2, (b) Ti_2AlC and (c) Cr_2AlC feedstock powders that are used in the cold spray experiments as overview (left: 500×) and in detail (right: 2000×)

Table 1 Particle sizes of the different MAX-powders used in cold spraying

Powder material	D10, µm	D50, µm	D90, µm
Ti_3SiC_2	23	42	67
Ti_2AlC	2	11	50
Cr_2AlC	2	9	23

equipped with a Quantax-200 energy-dispersive X-ray (EDX) micro-analysis system (Bruker Billerica, Massachusetts, USA) and a Quanta 650 from FEI-ThermoFisher Scientific. The morphologies of the MAX-phase powders and the single particle impacts were analyzed by a high-resolution SEM of type Helios G4 UC from FEI-Thermo Fisher Scientific.

Table 2 Material data used in calculations with the KSS software. Data are taken from the literature (Ref 28, 29, 31)

	Ti_3SiC_2	Ti_2AlC	Cr_2AlC
Uniaxial compressive strength (RT), MPa	1050	540	1160
Tm, °C	2670	1670	1530
Density, kg/m^3	4520	4110	5240
Cp, J/(kg K)	562	579	584

Table 3 Cold spray parameter sets using in the different MAX-phase deposition experiments

Layer type	Material	p_{gas}, bar	T_{gas}, °C	Traverse line speed, mm/s	Powder feed rate, cm^3/min
Single layer	Ti_3SiC_2	40	800	250	4.3
		40	900	250	4.3
		50	900	250	4.3
		50	1000	250	4.3
		50	1100	250	4.3
Single line "slow"	Ti_3SiC_2	50	1000	100	4.3
	Ti_2AlC				
	Cr_2AlC				
Single line	Ti_3SiC_2	50	1000	250	4.3
	Ti_2AlC				
	Cr_2AlC				
Single line "fast"	Ti_3SiC_2	50	1000	500	4.3
	Ti_2AlC				
	Cr_2AlC				
Wipe test	Ti_3SiC_2	50	1000	1000	0.43
	Ti_2AlC				
	Cr_2AlC				
Ten-layer coating	Ti_3SiC_2	50	1000	100	4.3
	Ti_2AlC				
	Cr_2AlC				

Substrate Surface Damage Data

A preliminary evaluation of substrate surface damage was performed by analyzing the cross sections of the single line deposits. For each spray condition, 20 particles were investigated. The damage ratio was then calculated by dividing the penetration depth of the particle into the substrate by the impacted particle's diameter.

Hardness Testing

Micro-hardness

Indentations on the polished cross sections of coating samples were performed using a Vickers indenter under a load of 1 N, utilizing a Micro-Combi depth-sensing indenter (Anton Paar TriTec, Corcelles, Switzerland). The dwell time was fixed to 15 s, while the loading and unloading rates were 2000 mN/min for a maximum load of 1 N and 6000 mN/min for 3 N. Ten indentations were performed on each sample.

Nano-hardness

Measurements of nano-hardness were taken on the same coatings with a Berkovich indenter, applying a maximum load of 10 mN, with a dwell time of 15 s and a loading/unloading rate of 20 mN/min. The tests were performed with NHT (Anton Paar TriTec) depth-sensing nano-indenter. On the Ti_2AlC and Cr_2AlC coatings, 15×15 matrices were performed to allow an analysis of data distribution. On the Ti_3SiC_2 coating, due to its lower thickness, 20 indentations were performed.

X-Ray Diffraction Analysis

The analyses of crystallographic structure were performed by X-ray diffraction using a D8 Discover diffractometer by Bruker, Billerica, Massachusetts, USA, with Cu K_α radiation with line focus and a 0.34° opened primary motorized optics and a 2.5° axial soller. The secondary beam path included a 2.5° axial soller with a Lynxeye_Xe_T detector. Data analyses were performed by using the Bruker DIFFRAC.SUITE EVA software. This software was also used to determine relative phase contents of powders and coatings.

Results

Particle Impact Conditions

To explore the possible differences of powder size and density on acceleration and heating during cold spraying,

the particle impact conditions were calculated by using the KSS software package. Respective data concerning impact temperature T_p and velocity v_p of Ti_3SiC_2, Ti_2AlC and Cr_2AlC particles are shown in Fig. 2. For cold spraying with a parameter set of p_{gas} = 50 bar and T_{gas} = 1000 °C, the velocities of the majority of spray particles vary over a rather small range between 700 and 850 m/s (Ti_3SiC_2: v_p = 699 to 801 m/s, Ti_2AlC: v_p = 717 to 802 m/s, Cr_2AlC: v_p = 733 to 849 m/s). Lower impact velocities of about 700 m/s are mainly obtained for the smallest species (D10) of the Ti_2AlC and Cr_2AlC size cuts, due to deceleration by the bow shock in front of the substrate, and the big Ti_3SiC_2 particles that reach lower velocities during the acceleration due to their large inertia. In contrast to impact velocities, the impact temperatures vary over a rather wide range from about 400 to 800 °C (Ti_3SiC_2: T_p = 602 to 813 °C, Ti_2AlC: T_p = 392 to 767 °C, Cr_2AlC: T_p = 444 to 762 °C). Since long powder injection distances (− 140 mm for Ti_2AlC and Cr_2AlC, − 205 mm for Ti_3SiC_2) up-stream of the nozzle throat were selected to guarantee sufficient heating time for all particles to reach the gas temperature, respective differences are attributed to cooling in the expanding regime of the de Laval nozzle and the free jet. By lower thermal inertia, smaller particles adapt more easily to the lower gas temperature than bigger ones. Thus, as compared to the other MAX-phase powders under investigation, the lower impact velocities and higher impact temperatures of Ti_3SiC_2 particles are due to their larger sizes. For illustrating the influence of cold spray parameters, the graph also shows respective impact conditions achievable by mean size (D50) of Ti_3SiC_2 particles for p_{gas} = 40 bar and T_{gas} = 800 °C, p_{gas} = 50 bar and T_{gas} = 900 °C, p_{gas} = 50 bar and T_{gas} = 1100 °C. The comparison demonstrates that, within this parameter regime, particle impact velocities and temperature are increased by about 90 m/s and 250 °C, respectively. Similar rises are observed for impact conditions of Ti_2AlC and Cr_2AlC, but not shown here. The comparison illustrates the need of high process gas temperatures to reach sufficiently high particle impact conditions for bonding.

In addition, Fig. 2 also includes the critical velocities as calculated by assuming a linear thermal softening behavior of typical metals. Since such approach over-simplifies the softening mechanisms of MAX phases, the calculated critical velocities can just give a rough guidance. The differences in critical velocities at low impact temperature are mainly attributed to the individual material strengths. The different slopes of critical velocities are due to their individual melting temperatures as derived from thermodynamic calculations and thus the assumed linear softening behavior. The crude comparison between impact conditions and respective critical velocities indicates that bonding conditions should be reached only by Ti_2AlC and Cr_2AlC, whereas the Ti_3SiC_2 powder velocities stay well below critical limits at respective impact temperatures. For direct comparison of optimum spray conditions, the ratio η between particle impact velocity and critical velocity at given impact temperature can be taken as a measure. Assuming the measured mean particle sizes of the powders and spray conditions with a pressure of 50 bar and a

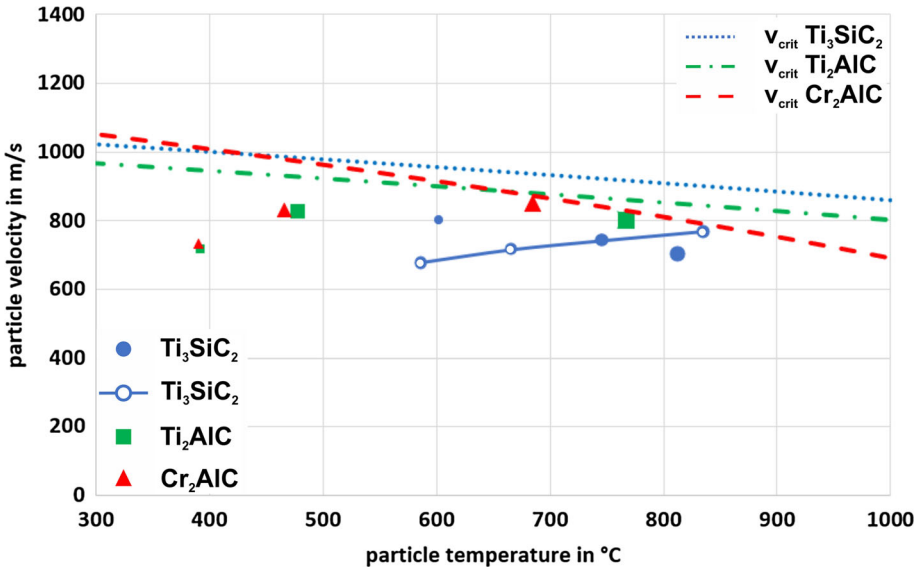

Fig. 2 Particle impact conditions for Ti_3SiC_2, Ti_2AlC and Cr_2AlC particles sprayed with 50 bar and 1000 °C, as calculated by using KSS software (dots). The small, middle and big symbol sizes correspond to the D10, D50 and D90 values according to Table 1, respectively. In addition, the impact conditions of D50 particle size for Ti_3SiC_2 are shown for cold spray parameter sets of p_{gas} = 40 bar and T_{gas} = 800 °C, p_{gas} = 50 bar and T_{gas} = 900 °C, p_{gas} = 50 bar and T_{gas} = 1100 °C (open dashed and solid circles, respectively). For comparison, critical velocities calculated by using standard models valid for metals are also shown (dashed lines)

temperature of 1000 °C, η was calculated to be 0.8 for Ti_3SiC_2, 0.89 for Ti_2AlC and 0.85 for Cr_2AlC, respectively. In reality, the differences might be larger due to the aberrant thermal softening and strain-rate hardening behavior of different MAX-phase materials. The later described significant difference in deposition behavior demonstrates that the situation is more complex, not only being influenced by types of possible deformation, but also by thermal influences (see discussion, description shown in Fig. 19) defining softening temperatures that will cause drastic changes in slopes of critical velocities.

Single-Layer and Single Line Deposit Microstructures

For distinguishing between coating deposition, possible erosion by particles impacting onto a previously deposited, hard and brittle MAX-phase layer as well as by spallation through internal cracks due to intrinsic stresses, the build-up of the different MAX-phase powders onto the substrates was studied in sequences of single spray lines, single layers and multiple layers for attaining suitable coating thickness.

Influence of Cold Spray Parameter Sets on Single-Layer Microstructures of Ti_3SiC_2 Deposits

In a series of preliminary experiments, three different powder sizes 2 to 16 µm (D50 = 7 µm), 12-35 µm (D50 = 21 µm) and 23-67 µm (D50 = 42 µm) were used for single-layer deposition (individual results are not given here). Since continuous surface coverage was only obtained by depositing the largest size, this powder was selected for subsequent experiments under systematic variation of process parameters. Figure 3 shows the microstructures of single-layer Ti_3SiC_2 deposits, cold-sprayed by different parameter sets with (a) 40 bar/800 °C, (b) 40 bar/900 °C, (c) 50 bar/900 °C, (d) 50 bar/1000 °C and (e) 50 bar/1100 °C. The deposition efficiencies (DE) under the different spray parameter sets were determined to be (a) DE = 4%, (b) DE = 4%, (c) DE = 6%, (d) DE = 6% and (e) DE = 4%, respectively. The stand-off distance, traverse speed and the line distance were set to 60 mm, 250 mm/s and 2 mm, respectively. The layers are highly non-uniform and reach a thickness of about 10 to 20 µm, nearly independent from the spray conditions. The interface between coating and substrate is rather rough, due to the deformation by the impacting Ti_3SiC_2 particles. The width of deformation pattern roughly corresponds to the initial particle diameters. In contrast, coating thickness and embedded layer parts are smaller than that. Thus, it can be assumed that the large individual particles, which impacted the substrate leaving coarse deformation pattern, subsequently fractured leaving smaller pieces present in the layer. All layers contain lateral cracks, but in different amounts. While most cracks spread through single splats, few others have lengths that reach up to 100 µm, thus covering more than one particle width. As indicated by the pattern in the substrate, the primary particles might stay intact at least during the impact, but might get fractured by subsequent ones. Any secondary or following impacts seem not to contribute to layer build-up. Within this comparison, the coating sprayed with a process gas pressure and temperature of 50 bar and 1000 °C, respectively, shows the lowest number of cracks, the most uniform layer and the highest DE within this comparison, albeit with a value of only about 6%. Thus, this spray parameter set was selected as reference for following experiments. Nevertheless, there remains some uncertainty, since it should be considered that, in the cold spray deposition of metals, the chosen powder feed rate should lead to a layer thickness of about 100-150 µm if the deposition efficiency is high.

Influence of Substrate Material and Traverse Robot Speeds on Single Line Deposit Features

For investigating the role of secondary impacts on splat or layer erosion, spray experiments by depositing single lines at different traverse speeds between 100 and 500 mm/s were performed on 304 steel and copper substrates. The choice of substrate materials of rather different mechanical strength should provide information on the role of particle deceleration on local stress development and fracture. For these experiments, the cold spray parameters are kept fixed at a pressure of 50 bar and a temperature of 1000 °C, according to the qualitative microstructural evaluation of the single layers presented in Fig. 3(d). Since local stress states, apart from substrate deformability, depend also on particle inertia and strength, these experiments are performed for all three MAX-phase powders under investigation.

Figure 4 shows the optical micrographs of the single line layers of Ti_3SiC_2 on 304 steel (left) and copper (right) sprayed with a traverse speed of (a) 100 mm/s, (b) 250 mm/s and (c) 500 mm/s. The comparison reveals the following:

(i) For all traverse speeds, the surfaces of the copper substrates are more deformed by particle impacts than the surfaces of the steel 304. Vice versa, particles impacting onto copper are less fractured than those on 304 steel. Thus, remnants of particles on steel at high traverse speed (500 mm/s) occur as thinner layer than those on copper. At complete surface coverage by adhering particles at slow traverse speed (100 mm/s), the layer on copper is less fractured and slightly thicker than that on steel.

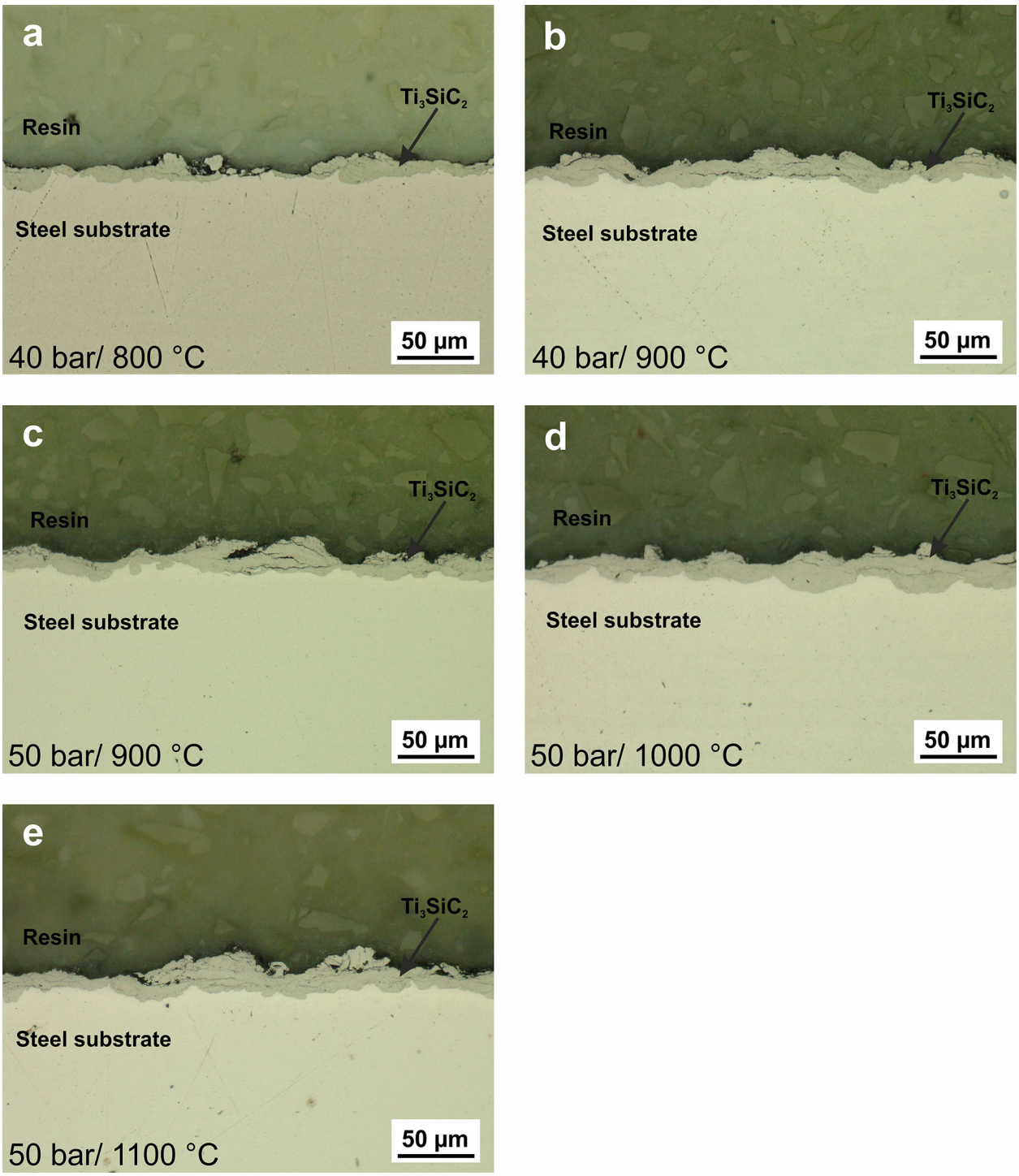

Fig. 3 OM micrographs showing the single-layer coating microstructures of Ti_3SiC_2 for cold spray conditions of (a) 40 bar/800 °C, (b) 40 bar/900 °C, (c) 50 bar/900 °C, (d) 50 bar/1000 °C and (e) 50 bar/1100 °C. The traverse line speed and the powder feed rate were set to 250 mm/s and 4.3 cm^3/min, respectively

(ii) The surface coverage by deposited particles is higher at slow traverse speed (100 mm/s) and could cause formation of a nearly closed layer, whereas faster traverse speeds result in independent single impacts, not all of them leading to bonding. However, none of the secondary impacts increases overall layer thickness. In contrast, any following impact seems to contribute to fracture of existing deposits.

The comparison thus demonstrates that local stress states by deceleration determine the degree of fracture of primary impacts on the substrate surface and that fracture is more enhanced if deceleration and stresses are higher, that is, if the surface is already covered by a Ti_3SiC_2 layer.

Figure 5 shows the optical micrographs of the single line layers of Ti_2AlC on steel (left) and copper (right), sprayed with 50 bar/1000 °C and a traverse speed of (a) 100 mm/s, (b) 250 mm/s and (c) 500 mm/s. As compared to the impact of Ti_3SiC_2 described above, the observations reveal similar trends:

(i) Copper substrate surfaces are more deformed than those of steel 304, and
(ii) At low traverse speeds better surface coverage and layer build-up by splats are obtained than by fast ones.

However, differences by choice of substrate material are less pronounced. Substrate deformation is generally lower than in the case of Ti_3SiC_2. Particularly, with respect to the appearance of fracture during deposition, the situation of Ti_2AlC is different to that of Ti_3SiC_2. In Ti_2AlC, the crack appearance in deposited particles is similar for copper and 304 steel substrates. For complete coverage at low traverse speed of 100 mm/s, the Ti_2AlC layer on the 304 steel substrate even appears more homogenous and less fractured by containing fewer cracks than that on copper, in this comparison indicating the beginning of coating formation.

Figure 6 shows the optical micrographs of the single line layer of Cr_2AlC on steel (left) and copper (right) sprayed with 50 bar/1000 °C and a traverse speed of (a) 100 mm/s, (b) 250 mm/s and (c) 500 mm/s. General features according to (i) the degree of substrate deformation, as well as (ii) surface coverage and associated particle or layer fracture, are similar to those occurring during deposition of Ti_2AlC. However, in contrast to Ti_2AlC, the deposition of Cr_2AlC allows for a more uniform and thicker layer build-up at slow traverse speeds of 100 mm/s, particularly being prominent on the copper substrate.

In summary, the comparison shows that the highest degree of substrate deformation can be observed for the Ti_3SiC_2 impacts, especially on the copper substrate. Under impacts of Ti_2AlC and Cr_2AlC, the steel substrate only shows very minor deformation. For impacts onto copper, Cr_2AlC causes slightly more surface deformation than does Ti_2AlC. At low traverse speeds ensuring multiple impacts, Cr_2AlC and Ti_2AlC can be built up as coatings, whereas Ti_3SiC_2 shows internal fracture and spallation.

Influence of Particle Size on Deformation by Substrate Surface Damage Ratios

To distinguish the role of particle sizes on substrate deformation, the ratios between penetration depth of the particle into the substrate and the individual particle diameters are determined on the basis of the single line deposits processed at high traverse speeds of 500 mm/s and process conditions with p_{gas} = 50 bar and T_{gas} = 1000 °C. Data for all materials are shown in Table 4. The respective impact ratios of the different MAX-phase powders used for cold spraying are rather similar.

Crystallographic Structures and Coating Microstructures

At the selected cold spray parameter set using a gas pressure of 50 bar and a gas temperature of 1000 °C, ten spray layers were applied to achieve a sufficiently high coating thickness for further investigations. In the following, details on crystallographic structures and microstructures of Ti_3SiC_2, Ti_2AlC and Cr_2AlC coatings are described in more detail.

Crystallographic Structures

Figure 7 compares the XRD patterns of the initial feedstock powders with those of corresponding Ti_3SiC_2, Ti_2AlC and Cr_2AlC coatings. For all three MAX-phase materials, the patterns of powder and coating are rather similar, demonstrating that initial structures of the powder are maintained during the deposition process. Thus, individual patterns mainly reveal possible impurities by the MAX-phase synthesis. The diffraction peaks of all MAX-phase coatings show slightly higher widths than the ones of respective powders, suggesting residual micro-strain due to plastic deformation at impact. This effect is more pronounced for Ti_3SiC_2.

The diffraction patterns of Ti_3SiC_2 are shown in Fig. 7(a) and reveal some small amounts of TiC (approx. 1% in the powder and 2% in the coating) in addition to the MAX-phase (approx. 99% in the powder and 98% in the coating). The pattern of the coating also indicates some amounts of the substrate material steel 304, which is due to a low coating thickness. As compared to the powder, the pattern of the coating shows different intensity distributions of the Ti_3SiC_2 phase, which could be attributed to a texture within the deposited layer. The texture could be due to preferred bonding of particles that hit the substrate surface with orientations that allow for plastic deformation by gliding systems activated on the basal planes, and fracture as well as rebounding of others.

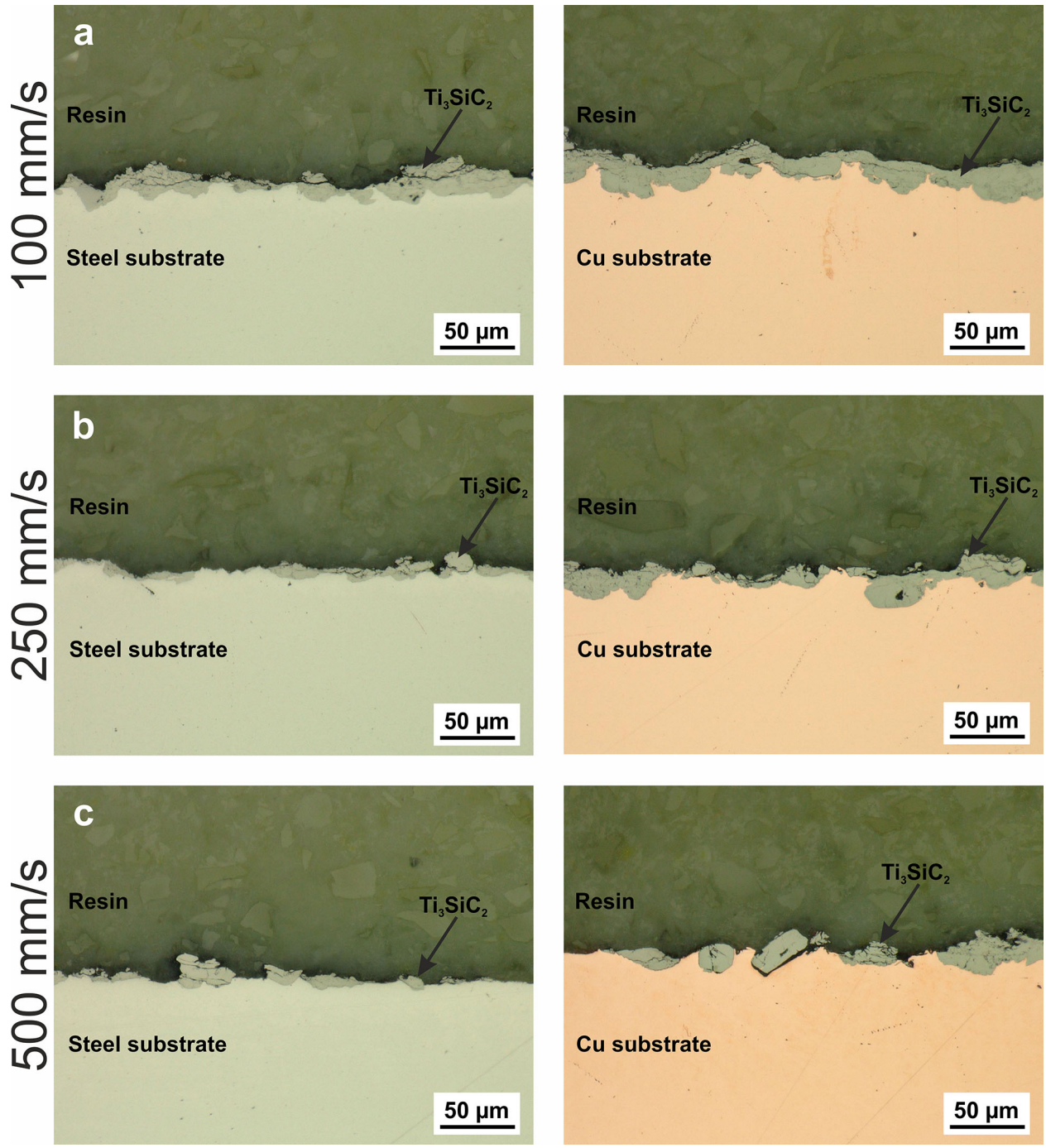

Fig. 4 OM micrographs showing single line layers of Ti_3SiC_2 on steel (left) and copper (right) sprayed with 50 bar/1000 °C and traverse speeds of (a) 100 mm/s, (b) 250 mm/s and (c) 500 mm/s. The powder feed rate was kept fixed at 4.3 cm^3/min

The XRD patterns of the Ti_2AlC powder and the cold-sprayed coating are shown in Fig. 7(b). In addition to Ti_2AlC (amounts of approximately 48% in the powder and 54% in the coating), the patterns reveal Ti_3AlC_2 as a second MAX phase (about 31% in the powder and 33% in the coating). In addition, small amounts of Ti_3AlC (less than 1% in the powder and coating) and Al_5Ti_2 (approx. 11% in the powder and 9% in the coating) are present. The relative peak intensities in powder and coating are similar.

Figure 7(c) compares the diffraction pattern of Cr_2AlC powder and coating. In addition to Cr_2AlC as main constituent (approx. 68% in the powder and 79% in the coating), chromium carbides such as Cr_7C_3 (approx. 17% in the powder and 10% in the coating) and Cr_3C_2 (approx. 16% in

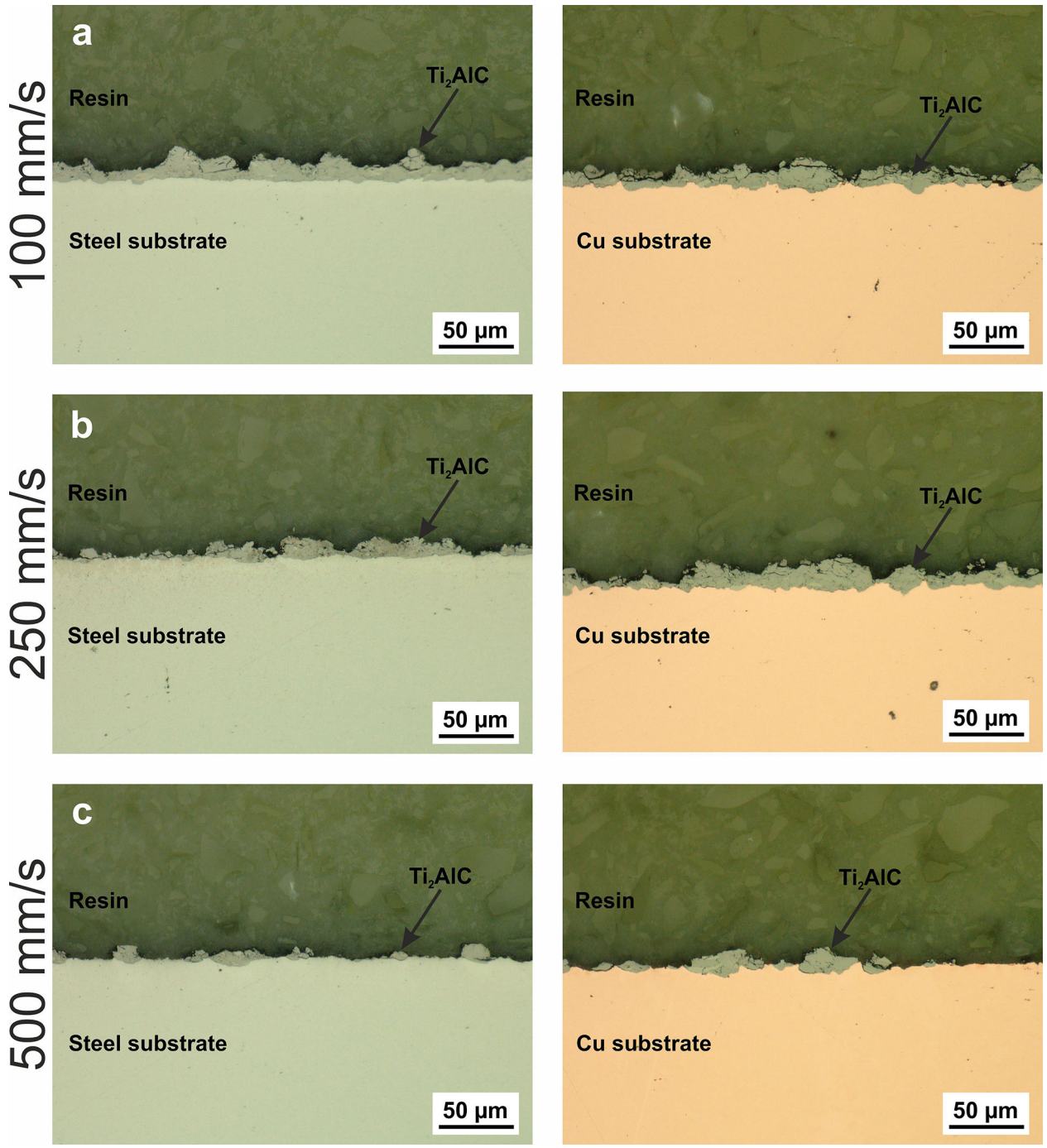

Fig. 5 OM micrographs showing the single line layers of Ti_2AlC on steel (left) and copper (right) sprayed with 50 bar/1000 °C and a traverse speed of (a) 100 mm/s, (b) 250 mm/s and (c) 500 mm/s. The powder feed rate was kept fixed at 4.3 cm^3/min

the powder and 12% in the coating) can also be identified as secondary phases. There remains some uncertainty about the carbide types, since most diffraction peaks of Cr_7C_3 overlap with those of the MAX-phase Cr_2AlC. Individual peak intensities of powder and coating are similar providing no hint for a possible texture.

With respect to above estimations of phase contents, it should be noted here that the Bruker DIFFRAC.SUITE EVA software just uses the peak heights for comparison. Thus, the given values should be treated with care and only serve for very rough orientation. Thus, some of the apparent differences in phase content between powders and coatings could just be a matter of the deformability of different phases. If plastic deformation builds up micro-strain in a phase, its peak widths (FWMH: full width at half-maximum height) increase and peak heights

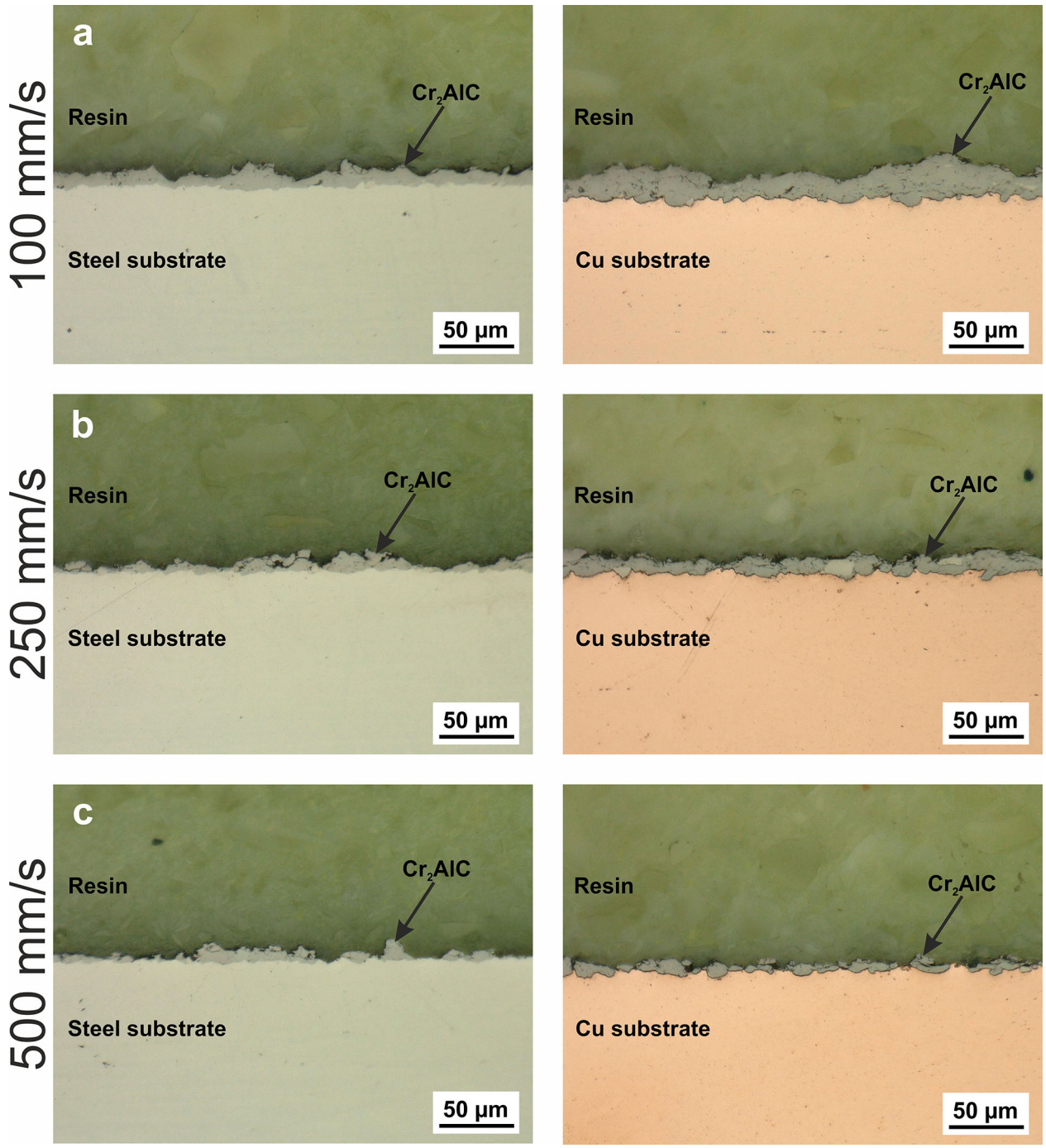

Fig. 6 OM micrographs showing the single line layer of Cr_2AlC on steel (left) and copper (right) sprayed with 50 bar/1000 °C and a traverse speed of (a) 100 mm/s, (b) 250 mm/s and (c) 500 mm/s. The powder feed rate was kept fixed at 4.3 cm^3/min

decrease, though the integrated intensities might remain the same.

Coating Microstructures

Figure 8 shows microstructure overviews of ten-layer coatings of (a) Ti_3SiC_2, (b) Ti_2AlC and (c) Cr_2AlC on steel, cold-sprayed at a gas pressure of 50 bar, a gas temperature of 1000 °C and a traverse speed of 100 mm/s. Details on the microstructures are given by the SEM micrographs in Fig. 9.

In case of Ti_3SiC_2, no continuous coating has formed (Fig. 8a, 9a). Adhering parts originate mainly from the primary impact events, then being fractured by following

Table 4 Substrate surface damage ratios for Ti_3SiC_2, Ti_2AlC and Cr_2AlC as obtained by processing single line deposits at high traverse speeds of 500 mm/s and process conditions with p_{gas} = 50 bar and T_{gas} = 1000 °C

Powder	Substrate	Damage ratio	SD
Ti_3SiC_2	Steel 304	0.24	± 0.08
	Copper	0.40	± 0.10
Ti_2AlC	Steel 304	0.20	± 0.07
	Copper	0.22	± 0.07
Cr_2AlC	Steel 304	0.22	± 0.08
	Copper	0.28	± 0.08

ones. Adhering parts reach a thickness of 45 µm at the most. The DE for the ten-layer Ti_3SiC_2 coating is < 1%. As shown in Fig. 9(a), the internal microstructures show high amounts of mainly lateral cracks. The poor deformability of Ti_3SiC_2 leads to failure in coating build-up and a decrease in DE with increasing layer number. It might be noted here in agreement to the results from single layer or single line build-up that the impact of Ti_3SiC_2 causes significantly more deformation of the 304 steel substrate than that during Ti_2AlC and Cr_2AlC coating formation.

Ti_2AlC is built up as rather thick coating (Fig. 8b, 9b) with a DE of nearly 10%. The thickness is rather non-uniform, varying from 300 to 530 µm, which is probably due to non-continuous feeding of this fine powder. In the homogenous parts, porosity is rather low (less than 5%). However, some parts show big voids with sizes of up to 100 µm. These are probably due to mechanical pull-outs caused by the sample preparation, indicating non-optimum internal cohesion. Microstructural details in Fig. 9(b) reveal mainly well bonded internal interfaces, but also a significant amount of mainly lateral cracks spreading along former intersplat boundaries reaching lengths of 50-100 µm. These cracks indicate that at least in some parts of the deposit, bonding is not optimum yet. The micrographs do not clearly show whether the mainly lateral crack orientation is dominated by compressive stresses or by weak bonds perpendicular to impact direction. The splats inside the coating appear to be flattened by the impact.

By the BSE mode of the SEM, phase impurities (here appearing in dark gray) are revealed. EDX analyses show that the darker inclusions are richer in Al (Fig. 10a, b-Spectrum 1) than the surrounding, brighter matrix (Spectrum 2). In agreement with the XRD patterns of the Ti_2AlC coating (Fig. 7b), it is inferred that the gray matrix corresponds to a mix of Ti_2AlC and Ti_3AlC_2, whereas the Al-rich areas consist of Al_5Ti_2 (titanium aluminide)

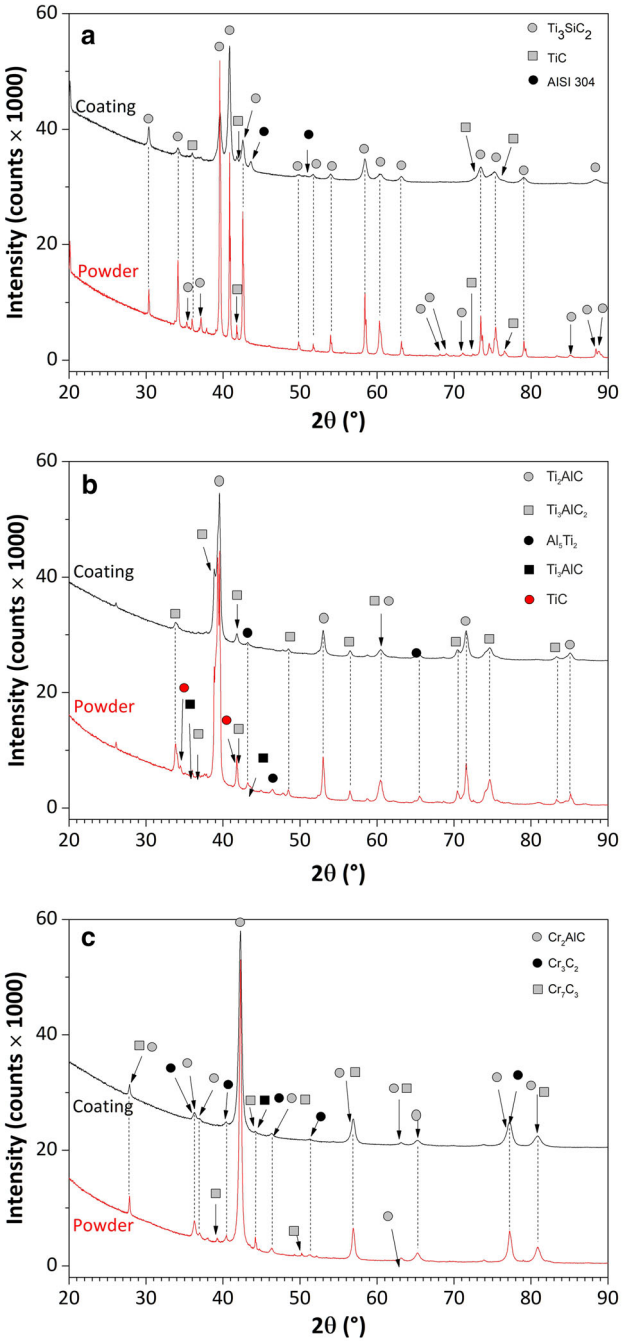

Fig. 7 XRD patterns of (a) Ti_3SiC_2, (b) Ti_2AlC and c) Cr_2AlC powder and coatings

inclusions. The latter is likely a leftover from the synthesis process.

Cold spraying of Cr_2AlC also results in coating build-up (Fig. 8c, 9c), and like for Ti_2AlC, the coating thickness is non-uniform and varies from 200 to 320 µm due to non-continuous feeding of these small-sized powder particles. According to the overview in Fig. 8(c), the coating shows rather low porosity of < 1%. The DE for the ten-layer Cr_2AlC coating is nearly 3%. The microstructural details

by SEM in Fig. 9(c) reveal locally varying features with low-porosity layers close to the interface with the substrate up to thickness of about 50 µm and more loosely bonded microstructure, with higher amounts of porosity, in the upper part of the coating. The dense layer close to the substrate interface shows flattened splats and lateral cracks like those of the Ti_2AlC coating. The more loosely bonded areas contain bigger, less flattened MAX-phase particles that are surrounded by smaller ones as well as by micropores, and only very few cracks.

The dense areas seem chemically homogeneous, as revealed by the mostly uniform BSE contrast level in SEM micrographs, whereas the non-uniform microstructures contain significant amounts of impurities (bright contrast). Based on EDX spectra (Fig. 10c, d-Spectrum 1), bright areas consist of Cr and C with practically no Al, unlike the surrounding matrix (Spectrum 2). In agreement with the XRD patterns (Fig. 7c), the bright Al-free inclusions are consequently identified as chromium carbides, embedded within a Cr_2AlC matrix. The non-flattened morphology of the bright carbide inclusions suggests that they existed as individual particles in the feedstock powder.

Since most of the pores seen in Fig. 10(c) have similar shape and size as the carbide inclusions, it could be argued here that respective porosity is caused by selective pull-out of these non-flattened carbide particles during polishing procedures, as they do not bond to the surrounding material during impact. So far, possible reasons for the different impurity amounts in the lower and the upper part of the coating cannot be distinguished in detail. One explanation for the non-uniformity of the Cr_2AlC coating can possibly reside in non-continuous powder feeding, sometimes resulting in particle clouds with higher mass loads. The vibrational mode of the powder feeder might have also induced the separation of different particle size fractions. However, it is not clear yet, why possible variations in powder feed rates should change impact conditions up to the point of making them selective for the bonding of distinct particles (e.g., favoring or hindering the bonding of chromium carbide-based particles, as it is seen in the different coating layers). Thus, in addition, effects by surface temperatures should be considered. Multilayer deposition increases the surface temperature of the coating and enhances surface deformability. Such could enable deposited MAX-phase layers to trap rather non-deformable, hard carbide particles by sorts of shear instabilities.

Coating Fracture

For revealing information on coating integrity and internal bonding, small strips were cut out from the samples and bent over a sharp edge to cause coating fracture. The respective fracture morphologies were analyzed by SEM.

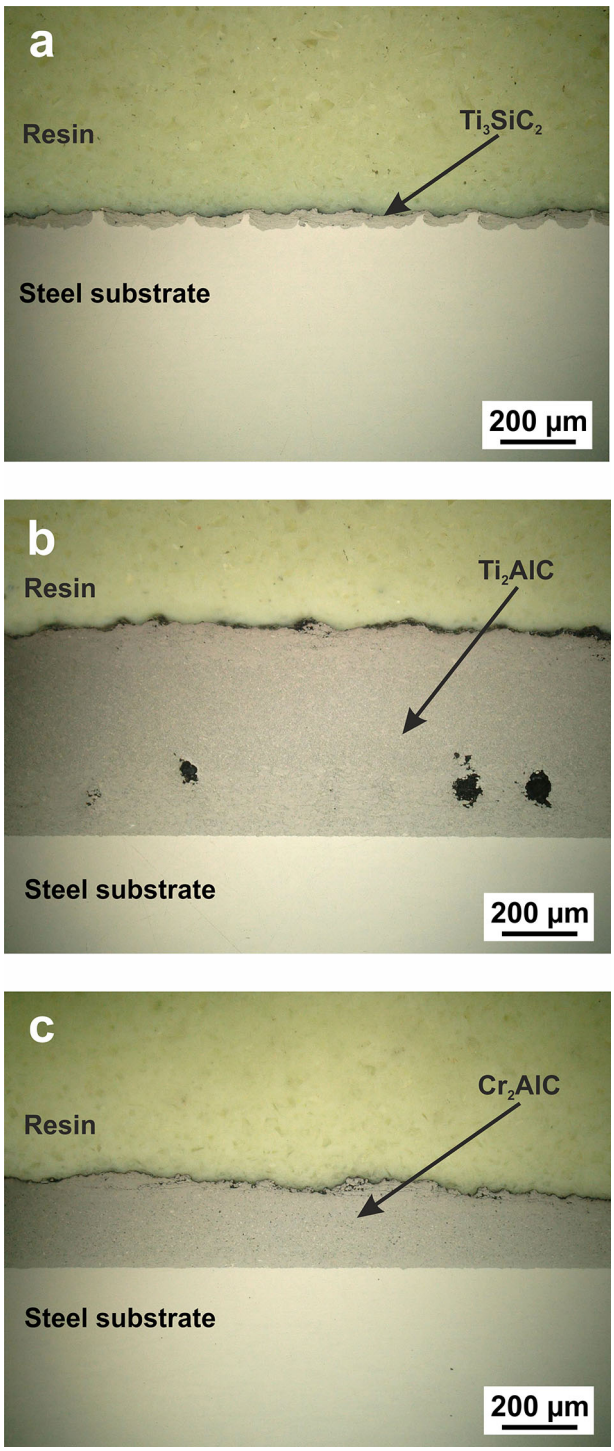

Fig. 8 OM micrographs showing the microstructures of ten-layer coatings of (a) Ti_3SiC_2, (b) Ti_2AlC and (c) Cr_2AlC on steel sprayed with 50 bar/1000 °C and a traverse speed of 100 mm/s. The powder feed rate was kept fixed at 4.3 cm^3/min

The respective results are shown in Fig. 11. The fracture morphologies of the Ti_3SiC_2 coating in Fig. 11(a) show flattened particles and delamination mainly along particle–particle interfaces. In some cases, also fracture going

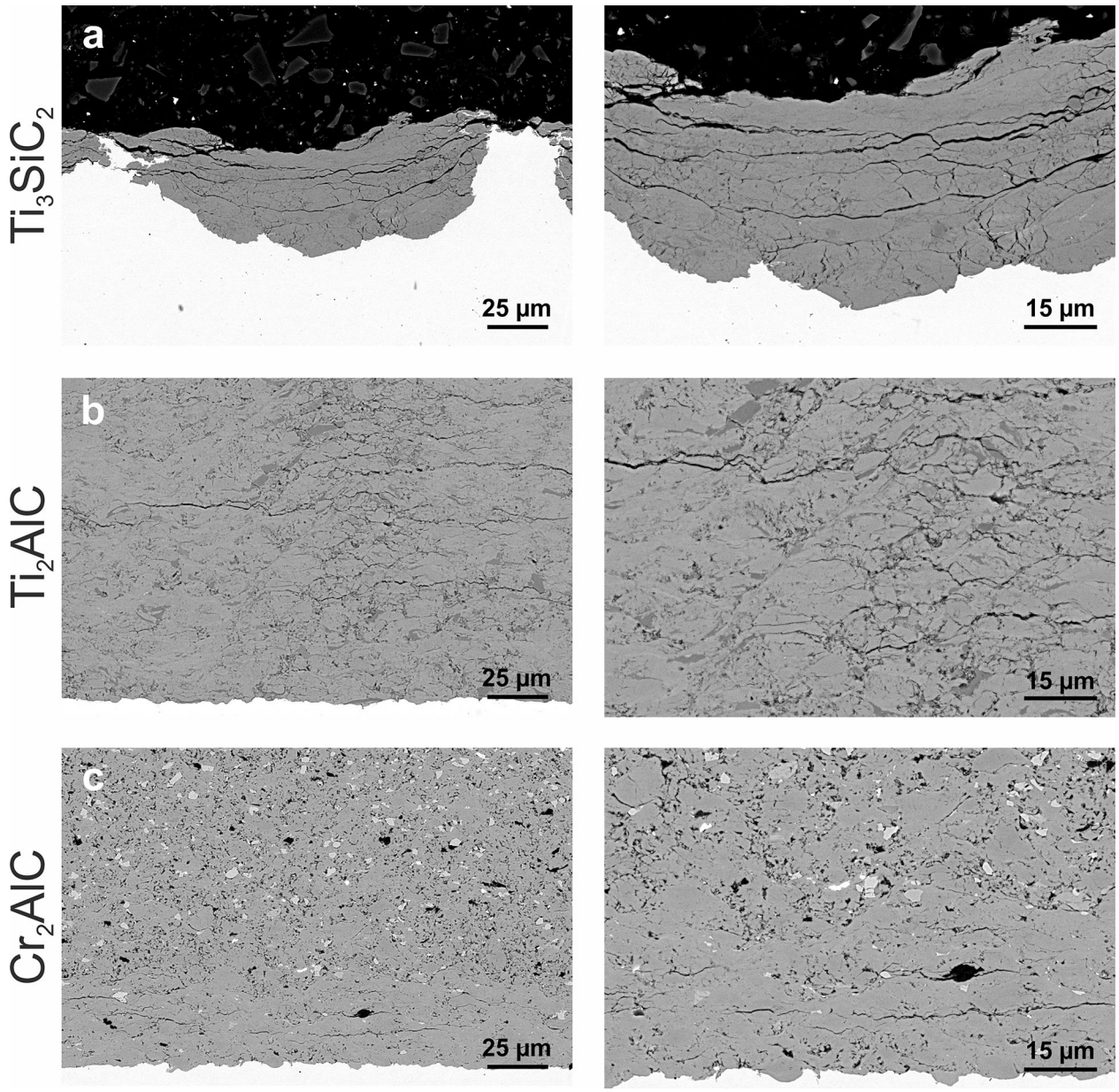

Fig. 9 SEM micrographs showing details of the ten-layer coating of (a) Ti_3SiC_2, (b) Ti_2AlC and (c) Cr_2AlC on steel sprayed with 50 bar/1000 °C and a traverse speed of 100 mm/s as overview (left: 2000×) and in detail (right, 4000×). The powder feed rate was kept fixed at 4.3 cm^3/min

through the splats can be observed, in these cases mainly following the path along and across the lamellar MAX-phase structure.

As shown in Fig. 11(b), the Ti_2AlC coating under bending spalls off from the substrate mainly in full layer thickness. According to the detailed view, most of the cracks seem to propagate through the interior of splats or particles, rather than along interparticle boundaries. The distinctive lamellae making up the MAX-phase structure are mainly oriented parallel to the coating/substrate interface within each flattened particle. The lamellae themselves show some bending and deformation. The fact that trans-splat fracture features are most prominent indicates a rather good coating integrity.

The fracture morphology of the Cr_2AlC coating is given in Fig. 11(c). The coating disintegrates with cracks mainly running parallel to the coating/substrate interface reaching a length of about 0.5 mm, indicating failure at locally less well bonded areas. Details of a more compact area indicate more prominently trans-granular/trans-splat failure. MAX-

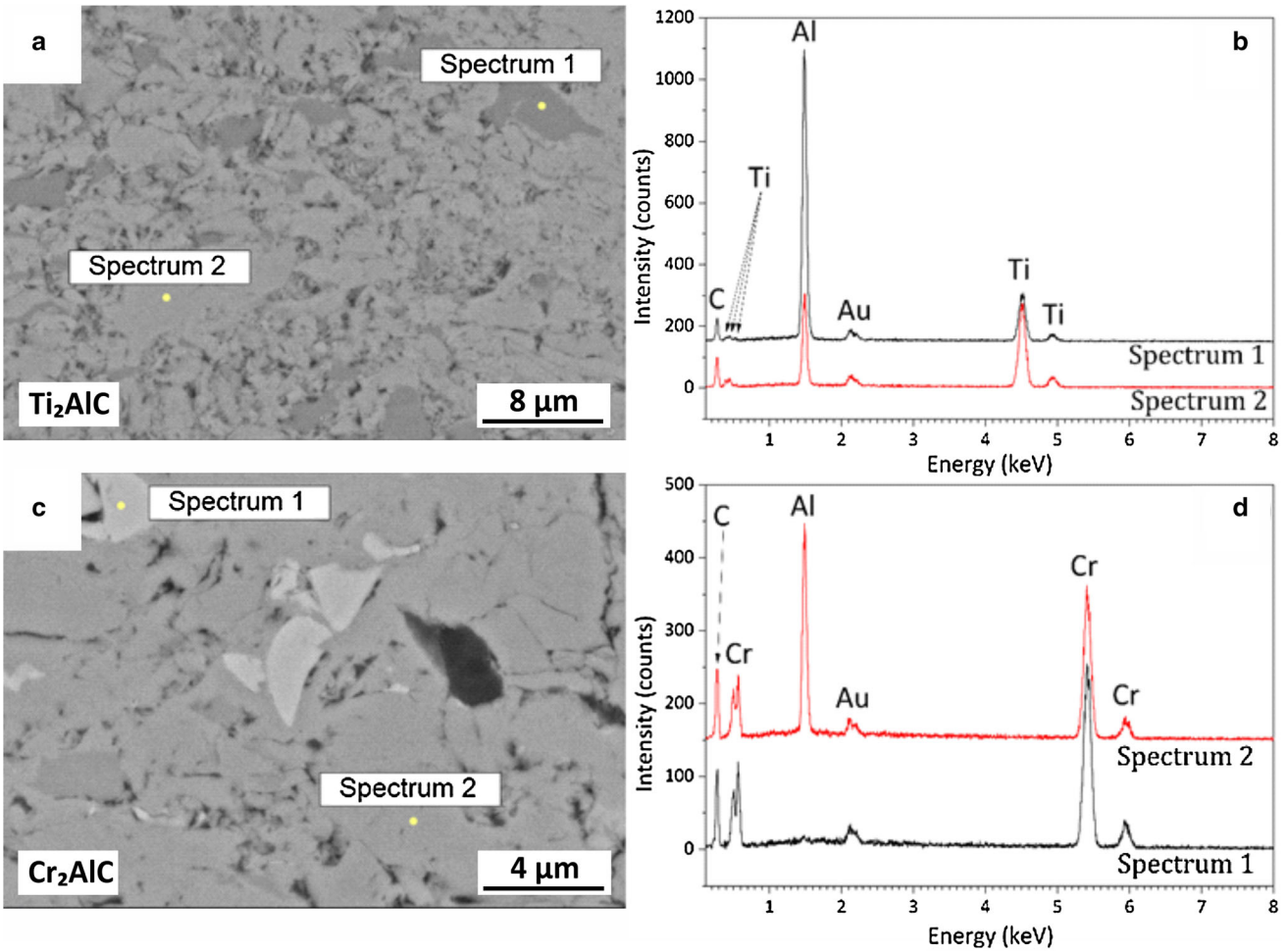

Fig. 10 SEM micrographs (backscattering electron contrast) of the Ti_2AlC (a) and Cr_2AlC (c) coatings on steel, with corresponding EDX spectra (b, d)

phase lamellas within the splats and grains are bent and show signs of plastic behavior. Their orientation has some preference for a direction parallel to the coating/substrate interface, but this orientation is less pronounced than it was in the Ti_2AlC coating. If local inhomogeneities could be avoided, the Cr_2AlC coating might show rather good integrity.

Coating Hardness

The micro-hardness values of the different coatings are shown in Table 5. Ti_3SiC_2 shows an average value of about 380 $HV_{0.1}$. Similar hardness values of about 380 $HV_{0.1}$ are obtained for Ti_2AlC. With about 590 $HV_{0.1}$, Cr_2AlC shows the highest micro-hardness. Nano-hardness values are notably higher than the micro-hardness (Table 5), which means micro-indentation results are largely affected by interparticle cohesion, while nano-indentation reflects the "intrinsic" material properties at intraparticle level. The nano-indentation load is indeed low enough that the resulting small indents are mostly confined within a single flattened particle.

All hardness data show statistical scatter. In case of the micro-hardness, this could be attributed to locally variable interparticle bonding strength as well as inhomogeneities between distinct layers of the coatings, as seen in Sect. 3.3.2. In fact, indenting the coatings in two adjacent layers, as shown in Fig. 12 for the case of Ti_2AlC, leads to very different indent sizes and micro-hardness values. The scatter among data obtained within a single coating layer is lower than the overall data scatter. In case of nano-hardness data, the large scatter can be attributed to chemically inhomogeneous inclusions as seen in Fig. 9 and 10.

Deeper investigation of the statistical distribution of nano-hardness data was carried out on Cr_2AlC and Ti_2AlC coatings, due to the large indentation matrix (15 × 15) performed on these samples. Respective data are summarized in Fig. 13. For Cr_2AlC, most of the nano-hardness values (Fig. 13a) are distributed around a median of approx. 1000 $HV_{0.001}$, but some are much larger, even >

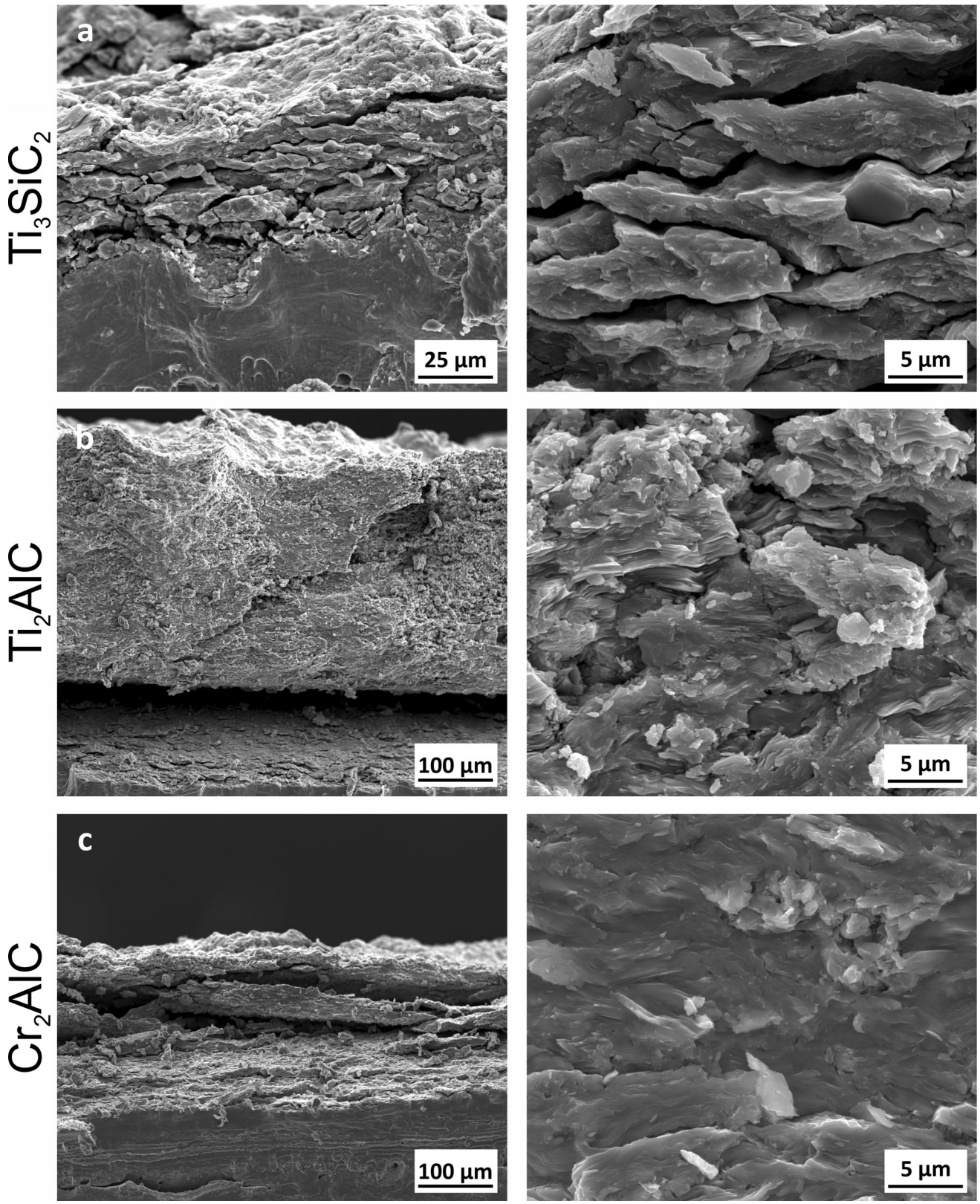

Fig. 11 Fracture morphologies of (a) Ti_3SiC_2, (b) Ti_2AlC and (c) Cr_2AlC coatings, cold-sprayed with p_{gas} = 50 bar and T_{gas} = 1000 °C, in overview (left) and detail (right). Where Ti_3SiC_2 disintegrates mainly at interparticle boundaries, the Ti_2AlC and (c) Cr_2AlC coatings most prominently show trans-granular/trans-splat fracture

Table 5 Micro- and nano-hardness values for Ti_3SiC, Cr_2AlC and Ti_2AlC MAX-phase coatings (average ± standard deviation)

	Ti_3SiC_2	Ti_2AlC	Cr_2AlC
Micro-hardness $HV_{0.1}$	383 ± 48	376 ± 115	585 ± 63
Nano-hardness $HV_{0.001}$	805 ± 420	893 ± 310	1153 ± 321

2000 $HV_{0.001}$. The SEM observations given in Fig. 14 show that some of the smallest nano-indentation marks fall onto the chromium carbide-based inclusions (Fig. 14-label 1) or half-way between these inclusions and the Cr_2AlC matrix (label 2). The hardness of Cr_3C_2 is listed as 2650 HV (Ref 32), which is consistent with the highest nano-hardness values obtained in this work. While part of the scatter in nano-indentation data is due to variability between the properties of individual Cr_2AlC flattened particles, the presence of some chromium carbide-based particles significantly contributes to this wide distribution. The very high hardness of these particles is also consistent with their lack of flattening (Fig. 9, 10).

The Ti_2AlC coating (Fig. 13b) shows a medium nano-hardness value of about 890 $HV_{0.001}$. The values range from < 500 $HV_{0.001}$ to $\approx$ 2000 $HV_{0.001}$, but no data points exceed 2000 $HV_{0.001}$. Accordingly, no hard carbide inclusions, comparable to the chromium carbide particles seen in the Cr_2AlC coating, appear in the Ti_2AlC sample. On the other hand, SEM investigation reveals especially big indents onto or near the dark inclusions (Fig. 15) that were identified as titanium aluminides in Sect. 3.3.2. Therefore, the aluminide inclusions probably account for the lowest hardness values in the distribution shown in Fig. 13(b).

Particle Impact Morphologies

For exploring cold spray phenomena, single impact morphologies as obtained by wipe tests supply vital information on local particle and substrate deformation as well as on possible failure modes. The SEM micrographs under angular view (tilted sample) in Fig. 16-18 show single impacts of Ti_3SiC_2, Ti_2AlC and Cr_2AlC, respectively, as obtained by cold spraying with p_{gas} = 50 bar and T_{gas} = 1000 °C onto steel 304 substrates. Since the number of particles on polished substrates for some samples was not sufficient to show all features, also some samples with non-polished substrate surfaces were chosen for the comparison. According to this comparison, depending on MAX-phase material, single particles adhere to different extent to the substrate and cause different deformation features. All given individual descriptions of these features were verified by subsequent EDX analyses of respective areas.

In the case of Ti_3SiC_2 shown in Fig. 16, most particles adhere leaving only few empty impact craters. More than half of the particles fracture during the impact. Bonded particles in most cases are flattened and show a splat like morphology, as indicated by (i) in Fig. 16(a). Interestingly, the substrate material shows pronounced jetting under the particle impact, an example given by (ii), which probably supports bonding. For completely fractured particles, see (iii, v) in panels a, b, c, it is not clear whether failure occurs along the characteristic shear planes of the MAX-phase structure or at grain boundaries. The laminar crystal structure is most prominently responsible for particle deformation, see (vi) in panels c, d, but it also causes internal delamination, see (vii) in panels b, d). In summary, despite the rather high impact and deformation temperature, the Ti_3SiC_2 particles show rather similar features as reported for conventional deformation and failure of MAX phases.

The particle impact morphologies of Ti_2AlC particles, given in Fig. 17, show slightly different features as compared to Ti_3SiC_2 with a larger amount of empty impact craters, particularly being more prominent for small sizes < 5 µm. The empty craters, however, show deformation features that indicate the formation of adiabatic shear instabilities (ASI) in the substrate material, see (ii) in (a), (b). Adhering particles are flattened, as indicated by (i) in a). Fracture or particle fragmentation seem to be of arbitrary nature, as shown by (iii) in (a), or cracks (v) in (b) and (c), not necessarily being associated to the lamellar MAX-phase structure. There are secondary impacts that adhere to primary ones (iv), given in (b) and (c). The details of related primary and secondary impacts indicate deformation features by slip along lamellas (vi) in (d). In addition to that, viscous-like deformation effects also occur along lamellar failure, see (vii) in (d).

Single impact events of Cr_2AlC, given in Fig. 18, in most cases result in adhering particles. Adhering particles are flattened as shown by (i) in (a). Only a limited number of small particles leave empty craters, in the present case disclosing adiabatic shear instabilities (ASI) of the substrate material as well, as indicated by (ii) in (a). Jetting of the substrate is observed only in very limited amounts. For Cr_2AlC, more than half of the particles seem to fracture, see (iii) in (a), (b). The respective cracks seem to proceed most prominently perpendicular to the lamella directions, see (v) in (c). However, it cannot be distinguished whether grain boundaries play a role for crack nucleation and growth. In most cases, internal lamellas are able to show plasticity-like deformation, as given by (vi) in (d). Secondary impacts can be bonded to primary ones, as shown by (iv) in (c). Associated with particle deformation, but also for interfaces between primary and secondary impacts, viscous-like flow can be observed, as indicated by (vii) in

(c) and (d). It might be noted that single, undeformed Cr_3C_2-particles stick into the substrate surface without any deformation, unlike the Cr_2AlC particles, see (viii) in (a).

Discussion

The results show that Ti_3SiC_2, Ti_2AlC and Cr_2AlC MAX-phase powders show rather different behavior during cold spraying. For Ti_3SiC_2, even the highest parameter set that should guarantee particle impact temperatures of about 800 °C did not lead to coating formation. Individual particles fractured during impact or by impacts of following particles. In contrast, Ti_2AlC and Cr_2AlC can be built up as coatings with rather low porosity. However, their overall appearance is still impaired by lateral cracks and local microstructure inhomogeneities. Thus, detailed analyses on crack formation and local difference in microstructure could supply the understanding for improving coating quality by subsequent powder design and respective tuning of cold spray conditions.

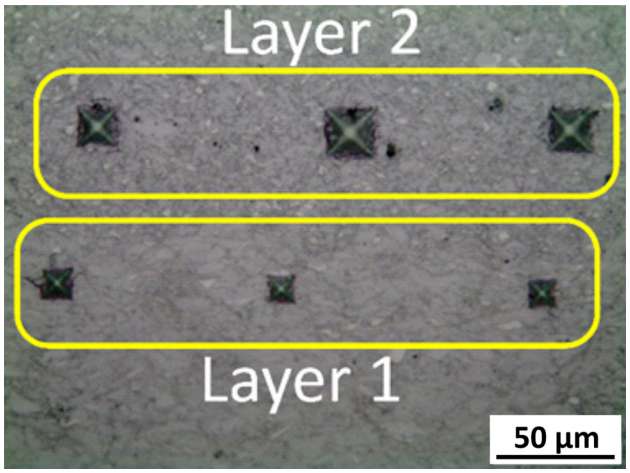

Fig. 12 Optical micrograph showing Vickers micro-indentations (1 N load) onto distinct layers of the Ti_2AlC coating

As seen in the layer build-up and descriptions of microstructures, the three MAX-phase powders Ti_3SiC_2, Ti_2AlC and Cr_2AlC show different characteristics during solid-state impacts in cold spraying. Various reasons could be responsible for different deformation features: (i) different particle impact conditions (normalized temperature and velocity) in cold spraying, (ii) different material density and particle sizes, leading to (iii) different inertia at impact that could cause surface damage, and (iv) different material properties like ultimate strength or flow stress, limiting deformation, and differences in thermal softening enabling plasticity. By applying the same process parameters and boundary conditions to the different MAX-phase powders, the possible roles of these factors may be distinguished.

For cold spraying with a gas pressure of 50 bar and a gas temperature of 1000 °C, for the mean sizes (D50), rather similar particle impact velocities of about 700 to 850 m/s are obtained according to the calculations. Therefore, addressing points (i) through (iii), despite the differences in particles sizes and thus mechanical and thermal inertia, all three MAX-phase materials are exposed to similar deceleration upon impact and, concomitantly, to similar primary deformation rates. Thus, individual material densities and particle sizes do not seem to play a major role for the observed differences in coating formation, as addressed in the following.

Focusing on (ii), the above conclusion is supported by analysis of the deformation topographies on metal substrate surfaces. Depending on MAX-phase material and powder, the primary impacts of particles onto the substrate cause

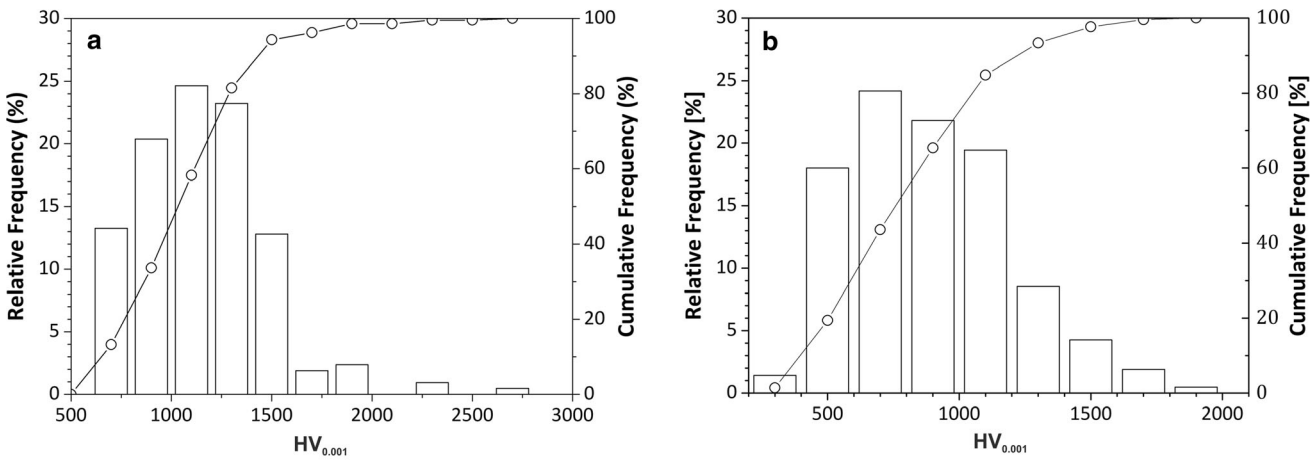

Fig. 13 Distribution of nano-hardness values measured through a 15 × 15 indentation matrix onto the cross section of (a) Cr_2AlC and (b) Ti_2AlC coatings: frequency count and cumulative probability

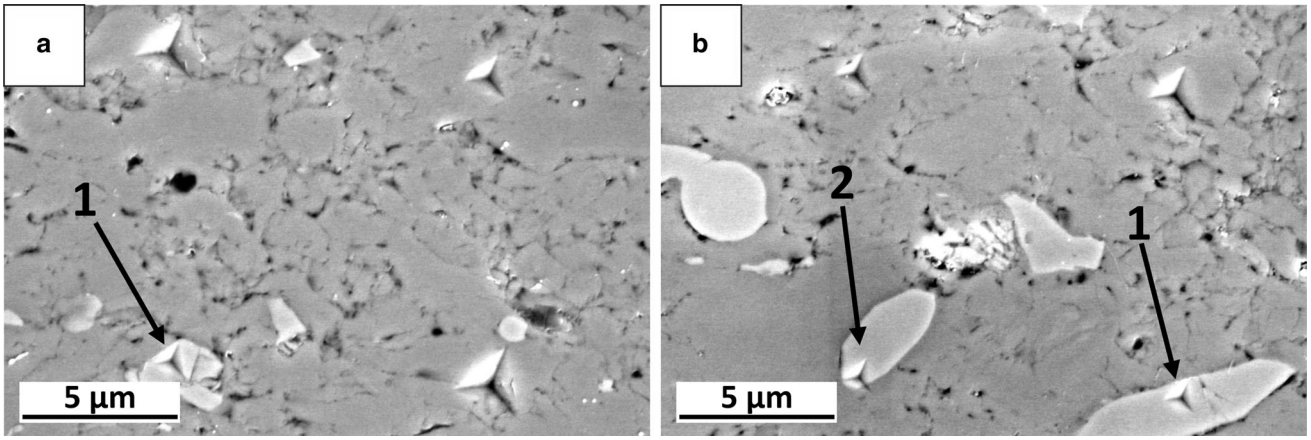

Fig. 14 SEM micrographs showing Berkovich nano-indentation marks on the cross section of the Cr_2AlC coating, especially highlighting small indents falling (i) onto the bright chromium carbide-based particles or (ii) at their interface with the surrounding Cr_2AlC matrix

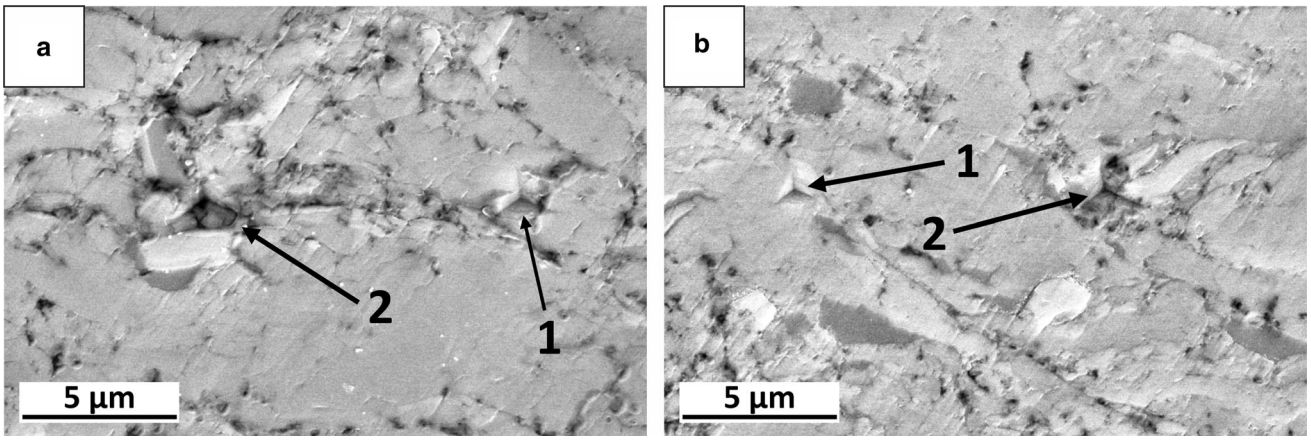

Fig. 15 SEM micrographs showing Berkovich nano-indentation marks on the cross section of the Ti_2AlC coating, especially highlighting small indents falling (1) at the interface between dark and bright inclusions with the matrix or (2) onto the matrix

different interface morphologies. It is indeed seen in Sect. 3.2.2 that bigger Ti_3SiC_2 particles produce more extensive deformation of both steel and copper substrate surfaces, in comparison with finer Ti_2AlC and Cr_2AlC particles. However, normalizing that as damage ratio (i.e., penetration depth/particle diameter) returns values that are largely independent of particle size. This means that the deformation effect scales linearly with the diameter of the impacting particle. This effect occurs despite the significant change in impact temperature as a function of particle sizes, as observed in Sect. 3.1. While impact velocities are quite similar, indeed, particle temperatures span a range of around 400 °C (Fig. 2). The wide temperature range is ascribed to thermal inertia, as explained in Sect. 3.1: Small particles tend to follow the temperature of the gas stream as it cools down upon expansion through the de Laval nozzle, while coarser particles better retain the heat and thus temperature they acquired in the pre-heating stage.

In typical cold spraying of conventional metals, the higher impact temperatures of larger particles are often beneficial, in comparison with the behavior of small (micrometer-sized) particles. Higher temperatures result in thermal softening, which reduces the corresponding critical velocity. If the particle is not too big, the reduction in critical velocity is enough to over-compensate the lower impact velocity of the particle itself and is therefore conducive to proper bonding.

In case of MAX phases, this seems not to be the case. The proportionality between deformation and particle size means the geometry of the deformed system remains self-similar. It is known that geometrically similar systems exhibit analogous strain and stress distributions. Therefore, it can be speculated that the stresses exerted on a ductile substrate by particles of various sizes are not much different, at least in these experiments, although impact temperatures are different. Thus, at least with respect to

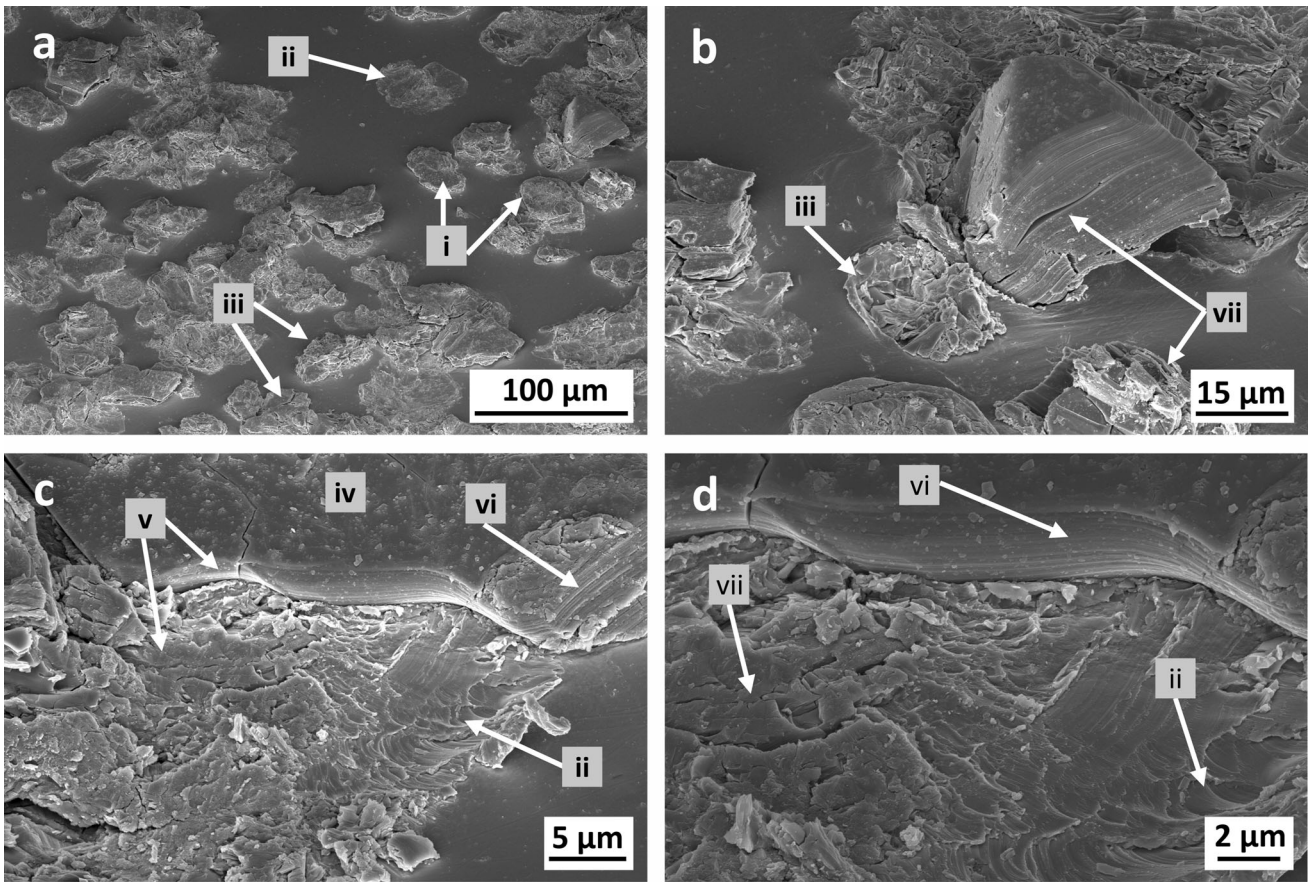

Fig. 16 Impact morphologies of Ti_3SiC_2 on steel 304 substrate as obtained by wipe tests by cold spraying with p_{gas} = 50 bar and T_{gas} = 1000 °C as analyzed by under angular view by SEM in different magnifications (a to d) allowing for overviews and detailed analyses. The individual indications were verified by EDX analysis. The inserts describe: (i: adhesion of complete, flattened particles, ii: crater with ASI of steel substrate, iii: fractured particles, iv: secondary particle impacts, v: cracks, vi: deformation on laminae, vii: fractured lamellas

stresses applied for substrate deformation, powder size should play a minor role.

To the contrary, particle sizes might play a role in the erosion of previously deposited coating layers, which is inferred from the severe erosion of the Ti_3SiC_2 layers as opposed to the thicker (though not damage-free) layers of Cr_2AlC and Ti_2AlC (Sect. 3.3.2).

The different responses observed when particles of different sizes impinge either on a metallic or ceramic surface (i.e., onto the substrate or onto the previously deposited MAX-phase layers) can be explained by the following rough estimations. In hardness testing, damage of ceramics is caused by lateral crack under unloading conditions, especially when the maximum applied force during the indentation stage exceeds a specific maximum threshold F_{max} as measure for local stress gradients (Ref 33). We can assume F_{max} = m * a = m * dv/dt, with m as particle mass, a as deceleration, v_p as particle velocity. Assuming that particles are decelerated to zero velocity (d$v = v_p - 0$), and estimating the time for deceleration as the time to deform the particle down to ¼ of the original particle diameter D_p leads to

$$\frac{dv}{dt} = \frac{v_p}{\frac{D_p}{4v_p}} = \frac{4v_p^2}{D_p}, \quad \text{(Eq 1)}$$

Thus, the locally applied force can be expressed as an inertia that by the assumptions has a dependence on the particle´s kinetic energy.

$$F = ma = \rho \frac{4\pi}{3} \left(\frac{D_p}{2}\right)^3 \frac{4v_p^2}{D_p} \quad \text{(Eq 2)}$$

For an estimate of the overall pressure under one particle, the maximum force can be normalized to the particle size with $p = F/A$, with

$$p = \frac{F}{\frac{\pi}{4} * (D_p)^2} \quad \text{(Eq 3)}$$

here A being the area under the impact.

Using the calculated data concerning particle impact velocity and respective input data on densities and sizes,

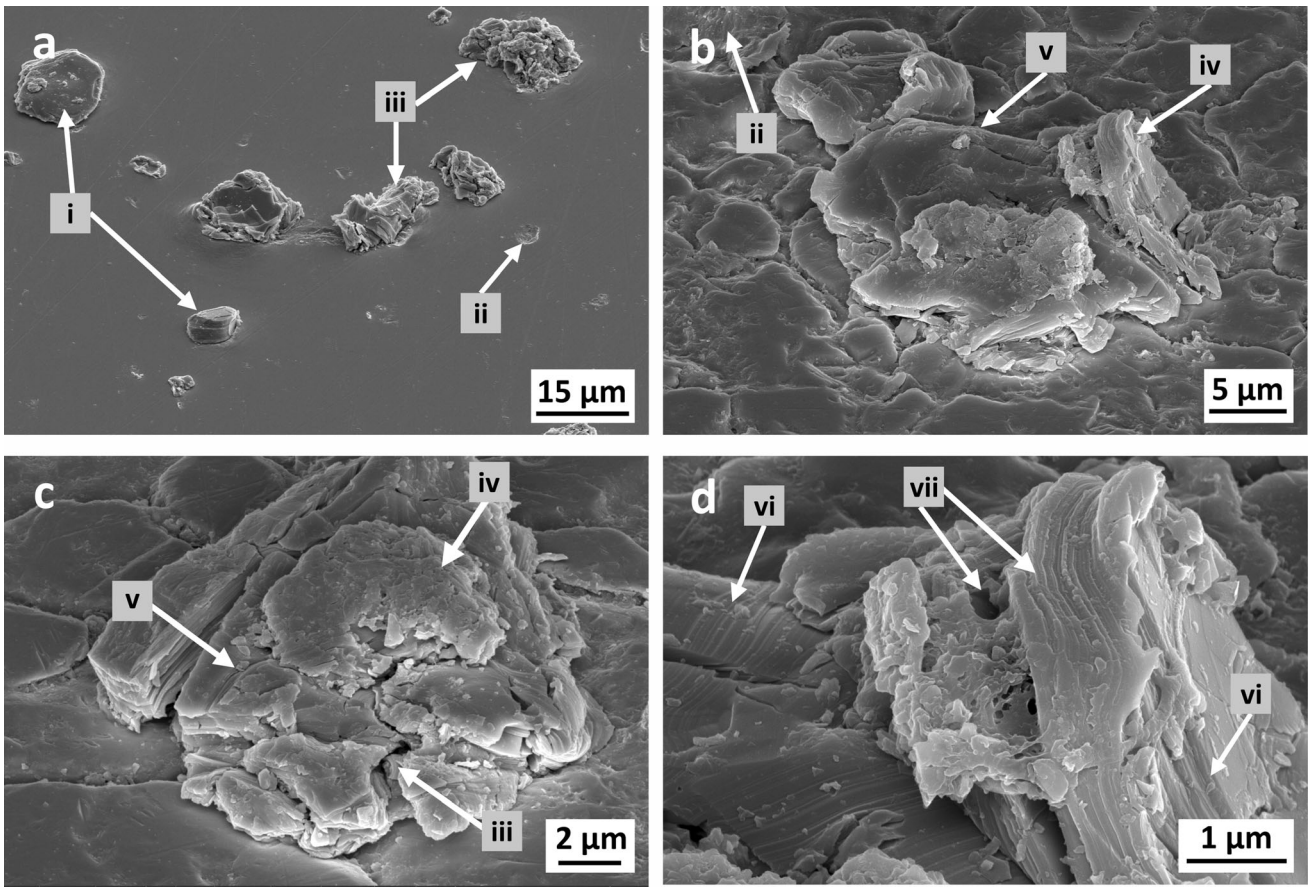

Fig. 17 Impact morphologies of Ti_2AlC on steel 304 substrate as obtained by wipe tests by cold spraying with p_{gas} = 50 bar and T_{gas} = 1000 °C as analyzed by under angular view by SEM in different magnifications (a to d) allowing for overviews and detailed analyses. The individual indications were verified by EDX analysis. The inserts describe: i: adhesion of complete, flattened particles, ii: empty impact crater with ASI of steel substrate, iii: fractured particles, iv: secondary particle impacts, v: cracks, vi: deformation on laminae, vii: viscous-like flow at laminae

F_{max} and p_{max} can be calculated. The respective comparison is given in Table 6. The comparison shows that applied pressures under the impact are rather similar. Considering all the rough assumptions of this estimate, this can be considered as good agreement to attained surface damage ratios on metal substrates, discussed above.

However, for a non-ductile substrate, the particle does not distribute the contact force over a contact area of the magnitude of A, as opposed to the above estimations. Neither the particle nor the substrate possesses enough deformability to conform well to one another. In this case, the particle inertia directly gets transformed into a local force exerted onto a very small area, and since F_{max} values might differ by nearly an order of magnitude, so do the associated stresses. Such might be the more reasonable situation for spraying onto a ceramic layer (e.g., a previously deposited MAX-phase layer) and might be considered as the cause for possible erosive features. It is noted here that all the assumptions neglect particle deformation. More details might be revealed in the near future by finite element analyses of the impact of MAX-phase particles.

For addressing (iv), the results show that for the analyzed cases of Ti_3SiC_2, Ti_2AlC and Cr_2AlC MAX phases, a significant number of cold-sprayed particles flattens upon impact, indicating plasticity-like or pseudo-plastic deformation. However, in deeper detail, the deformation features of the three MAX-phase materials differ significantly. Ti_3SiC_2 is most prone to fracture, occurring also across laminae, through layer delamination and kink banding. In contrast, Ti_2AlC and Cr_2AlC particles show more plastic deformation and slip along the laminae, i.e., along basal planes of the layered structure. In cases of Ti_2AlC and Cr_2AlC, even features of viscous-like flow can be observed along the laminae and at particle–particle interfaces, supporting deformation and bonding. Such features are not obtained for Ti_3SiC_2 impacts.

These experimentally observed differences may be explained by the strength and thermal softening behavior of individual MAX phases. According to literature data

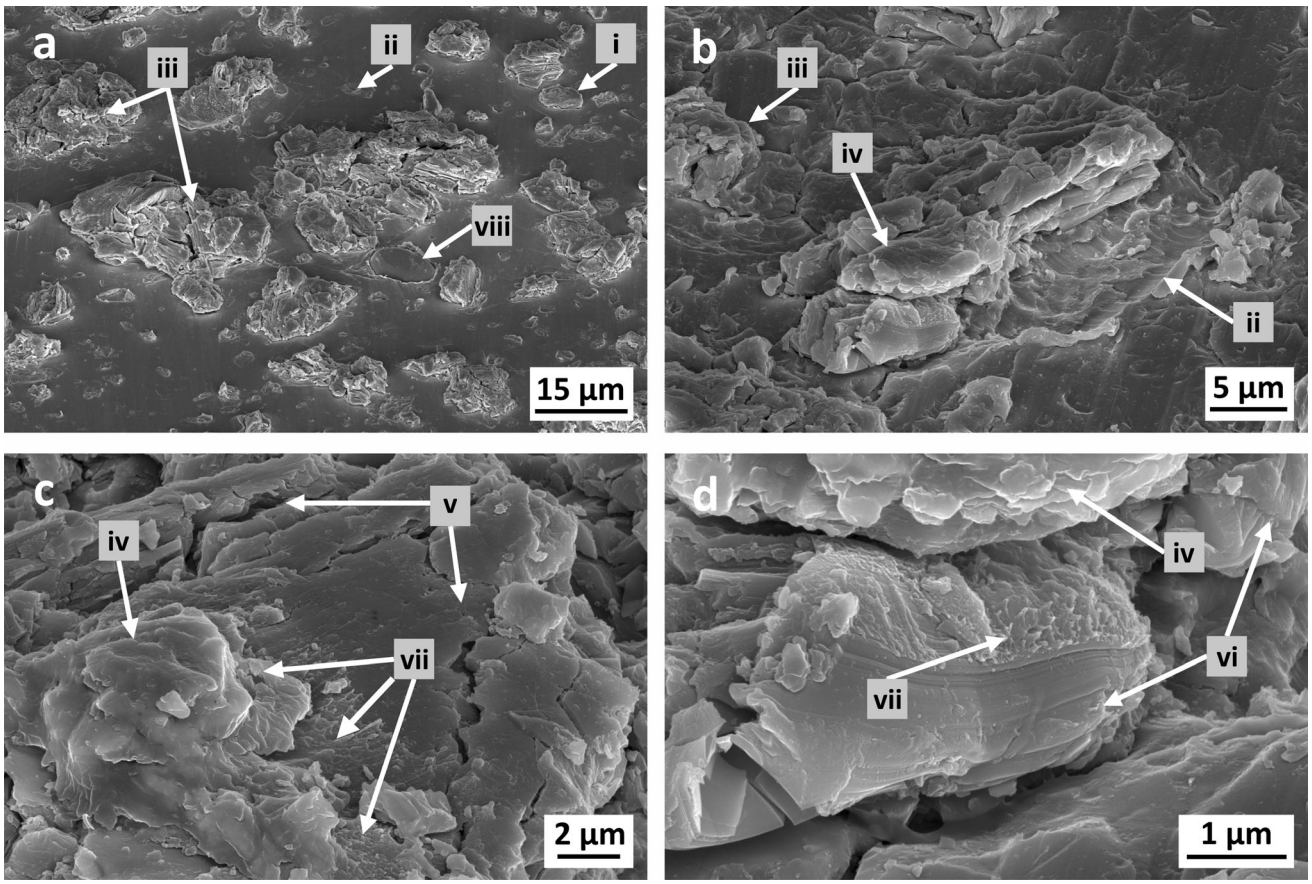

Fig. 18 Impact morphologies of Cr_2AlC on steel 304 substrate as obtained by wipe tests by cold spraying with p_{gas} = 50 bar and T_{gas} = 1000 °C as analyzed by under angular view by SEM in different magnifications (a to d) allowing for overviews and detailed analyses. The individual indications were verified by EDX analysis. The inserts describe: i: adhesion of complete, flattened particles ii: empty impact crater with ASI of steel substrate, iii: fractured particles, iv: secondary particle impacts, v: cracks, vi: deformation on laminae, vii: viscous-like flow at laminae, viii: Cr_3C_2-particle

replotted in Fig. 19 (Ref 29), Ti_2AlC has the lowest uniaxial compressive strength (UCS) of 560 MPa, in agreement to the present hardness tests. But up to about 1000 °C, the UCS does not change much and only slightly decreases at higher temperatures. The room temperature UCS of Ti_3SiC_2 and Cr_2AlC is rather high with values of 950 MPa for Ti_3SiC_2 and 1000 MPa for Cr_2AlC, respectively. Further, the UCSs of both Ti_3SiC_2 and Cr_2AlC decrease constantly down to 690 MPa and 750 MPa at 800 °C, respectively. Above this temperature, however, a difference emerges. The UCS of Ti_3SiC_2 only shows a minor decrease, whereas the UCS of Cr_2AlC softens to less than 600 MPa at 900 °C, similar to the strength of Ti_2AlC. This means that the thermal softening and the plasticity of the MAX phases at higher temperatures, rather than their room temperature strength, are decisive for possible coating formation. With particle impact temperatures of about 400 to 800 °C, even for Ti_2AlC and Cr_2AlC, additional heat sources are needed to achieve sufficient deformation for bonding.

As shown by the single impact phenomena, Ti_2AlC and Cr_2AlC locally show viscous-like deformation. This is not observed for impacts of Ti_3SiC_2. The difference can be explained by dislocation-like plastic deformation being prominent for Ti_2AlC and Cr_2AlC, and strain-rate hardening playing a minor role, in agreement to the literature (Ref 5). In contrast, for Ti_3SiC_2 thermal softening is less pronounced; moreover, the change in deformation mechanisms results in large strain hardening effects (Ref 30).

Table 6 Estimated max forces F_{max} and pressures p_{max} applied by the mean particle sizes (D50) under the impact conditions of the different MAX-phase material powders during cold spraying at p_{gas} = 50 bar, T_{gas} = 1000 °C

Material	v_p (D50), m/s	F_{max} (D50), N	p_{max} (D50), GPa
Ti_3SiC_2	741	8.970	6.6
Ti_2AlC	828	0.769	7.5
Cr_2AlC	831	0.576	9.6

Thus, the associated features in high-velocity impacts even at high temperatures are similar to those of brittle ceramics.

In addition to general MAX-phase properties, phase impurities by material synthesis can also have an influence on coating formation and possible properties. Some of these influences can be discussed on the basis of hardness data.

Comparison between the micro-hardness data of the present coatings and corresponding bulk materials (where available) systematically reveals large differences. For instance, the hardness of the Ti_3SiC_2 coating is lower than the ones reported by El Raghy et al. (Ref 34) for the respective bulk material (8 GPa for similar loads (Ref 34)). Analogously, the micro-hardness of the Ti_2AlC coating is lower than the bulk micro-hardness results (5.5 GPa) (Ref 35).

On the other hand, micro-hardness values generally agree well with those of other thermal-spray MAX-phase coatings. For example, the micro-hardness of the cold-sprayed Ti_2AlC coating agrees well with that of HVOF-sprayed coatings (Ref 16). The cold-sprayed Cr_2AlC coating shows the highest micro-hardness among the present samples, and it is comparable to the one found by Zhang et al. (Ref 36) for plasma-sprayed layers. A discrepancy only emerges between the micro-hardness of the cold-sprayed Ti_3SiC_2 coating and the values reported by El Raghy et al. (Ref 34) for APS Ti_3SiC_2 (600-1900 $HV_{0.05}$), but this might be attributed to the fact that the main phase of the APS coating in the cited reference was actually TiC, with Ti_3SiC_2 only detectable as a minor phase.

Moreover, the nano-hardness values of the cold-sprayed coatings are remarkably higher than the corresponding micro-hardness values. In this case, the nano-hardness of the Ti_2AlC coating is similar to that of the corresponding bulk material (8.24 GPa) (Ref 37).

Overall, these comparisons prove that, at the nanoscale, MAX-phase properties are retained during cold spraying, but macroscale properties (revealed by micro-indentation) are degraded by imperfect interparticle cohesion, which results in interparticle failure. This is true even for the Ti_2AlC and Cr_2AlC coatings, despite the somewhat better deformability exhibited by individual particles. Thus, for attaining high-quality MAX-phase coatings by cold spraying, further optimization of the deposition process (including adjustments to the particle synthesis and classification procedures) is probably required in order to exploit the better deformability of these materials to full advantage. Moreover, improved phase purity is also desirable: Local property variations at the nanoscale, indeed, occur due to the presence of impurities, as shown by the nano-hardness distributions and by the related SEM inspection of nano-indentation marks.

Summing up all given results and correlations, the present study is a first step to gain the needed overview on most influential properties of MAX-phase materials and prerequisites for powder design as well as cold spray conditions.

Summary and Conclusions

The present study shows that Ti_2AlC and Cr_2AlC MAX-phase coatings can be deposited by cold gas spraying. Ti_3SiC_2, by contrast, seems to be unsuitable for cold spray processing, despite all parameter and powder size variations (not all of which have been shown here).

An analysis of individual particles collected onto metallic substrates shows that their size probably has limited effect on the deposition behavior of the first coating layer, though large particles might promote erosion of previously deposited layers. The respective high strain-rate deformation mechanisms of MAX phases, therefore, seem to play a major role in coating formation. The impact morphologies indicate that Ti_2AlC and Cr_2AlC show some thermal softening, locally leading to viscous-like flow and, probably, enhanced interparticle bonding. This was corroborated by literature data on the evolution of compressive strength with temperature. Namely, when heated by the process gas, both materials attain similarly low compressive strength values, which explains their plastic deformability. It is likely that further heating upon impact results in the observed viscous-like behavior.

In contrast, Ti_3SiC_2 behaves more similar to brittle ceramics, though it exhibits some typical features of MAX-phase deformation. Indeed, even at the highest temperatures currently attainable through cold-spray systems, its compressive strength is reportedly high, thus limiting the deformability of individual particles.

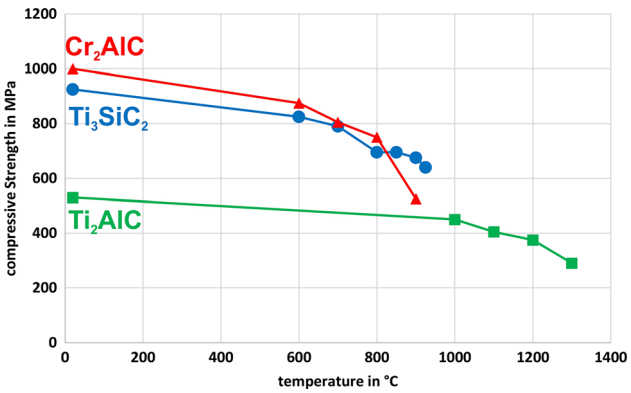

Fig. 19 Effect of temperature on uniaxial compressive strength (UCS) for Cr_2AlC, Ti_3SiC_2 and Ti_2AlC, redrawn according to (Ref 29)

Indentation analysis reveals that deposited particles retain the same nanoscale properties as the corresponding bulk MAX phases, consistent with the absence of phase alteration in XRD patterns. However, macroscale properties, even those of thick Ti_2AlC and Cr_2AlC coating, are degraded by limited interparticle cohesion. Therefore, despite the observed deformation and viscous-like behavior, impact conditions of these MAX-phase particles need further optimization.

In summary, the present study allows to derive general rules on MAX-phase selection for suitability in cold spraying, and also for defining needs according to cold spray parameter sets as well as the selection of powder sizes. Thus, the comparison of the behavior of different MAX phases in cold spraying could be interpreted as the first comprehensive step to tune this class of materials for future applications.

Acknowledgments The authors would like to thank the laboratory staff of the Helmut-Schmidt-University, Thomas Breckwoldt, Marion Kollmeier, Stefan Meier, Matthias Schulze and Camilla Schulze. The authors greatly acknowledge financial support of the EU project "IL TOVATORE" under Grant Agreement No 740415. In addition, we would like to thank our project partners Erik Ström, Sandvik Heating Technology, Hallstahammar, Sweden for powder supply, Jozef (Jef) Vleugels, KU Leuven Heverlee, Belgium and Peter Polcik, Plansee Composite Materials GmbH, Lechbruck am See, Germany, for powder milling, as well as Moritz to Baben, GTT-Technologies, Herzogenrath, Germany, for calculation of MAX-phase melting temperatures.

Funding Open Access funding enabled and organized by Projekt DEAL.

References

1. M.W. Barsoum and T. El-Raghy, The MAX-Phases: Unique New Carbide and Nitride Materials, *Am. Sci.*, 2001, **89**, p 334-343
2. Y. Zhou and Z. Sun, Electronic Structure and Bonding Properties of Layered Machinable Ti_2AlC and Ti_2ALN Ceramics, *Phys. Rev. B*, 2000, **61**(19), p 12570-12573
3. M. Radovic, M.W. Barsoum, and M.A.X. Phases, Bridging the gap Between Metals and Ceramics, *Am. Ceram. Soc. Bull.*, 2013, **92**(3), p 20-27
4. C. Brüsewitz, I. Knorr, H. Hofsäss, M.W. Barsoum, and C.A. Volkert, Single Crystal Pillar Microcompression Tests of the max phases Ti_2AlC and Ti_4AlN_3, *Scripta Mater.*, 2013, **69**, p 303-306
5. R. Bhattacharya, R. Benitez, M. Radovic, and N.C. Goulbourne, High Strain-Rate Response and Deformation Mechanisms in Polycrystalline Ti_2AlC, *Mater. Sci. Eng., A*, 2014, **598**, p 319-326
6. E. Drouelle, A. Joulain, J. Cormier, V. Gauthier-Brunet, P. Villechaise, S. Dubois, and P. Sallot, Deformation Mechanisms During High Temperature Tensile Creep of Ti_2AlC_2 MAX Phase, *J. Alloy. Compd.*, 2017, **693**, p 622-630
7. Y. Wada, N. Sekido, T. Ohmura, and K. Yoshimi, Deformation Microstructure Developed by Nanoindentation of a MAX Phase Ti_2AlC, *Mater. Trans.*, 2018, **59**(5), p 771-778
8. M.W. Barsoum, The $M_{n+1}AX_n$ Phases: a New Class of Solids: Thermodynamically Stable Nanolaminates, *Prog. Solid State Chem.*, 2000, **28**, p 201-281
9. A.S. Farle, C. Kwakernaak, S. van der Zwaag, and W.G. Sloof, A Conceptual Study into the Potential of $M_{n+1}AX_n$-Phase Ceramics for Self-healing of Crack Damage, *J. Eur. Ceram. Soc.*, 2015, **35**, p 37-45
10. M. Sundberg, G. Malmqvist, A. Magnusson, and T. El-Raghy, Alumina Forming High Temperature Silicides and Carbides, *Ceram. Int.*, 2004, **30**, p 1899-1904
11. D.J. Tallman, B. Anasori, and M.W. Barsoum, A Critical Review of the Oxidation of Ti_2AlC, Ti_3AlC_2 and Cr_2AlC in Air, *Mater. Res. Lett.*, 2013, **3**, p 115-125
12. Z.M. Sun, Progress in Research and Development on MAX Phases: A Family of Layered Ternary Compounds, *Int. Mater. Rev.*, 2011, **56**(3), p 143-166
13. C. Walter, C. Martinez, T. El-Raghy, and J.M. Schneider, Towards Large Area MAX Phase Coatings on Steel, *Steel Res. Int.*, 2005, **76**(2/3), p 225-228
14. P. Eklund, M. Beckers, U. Jansson, H. Högberg, and L. Hultman, The $M_{n+1}AX_n$ Phases: Materials Science and Thin-Film Processing, *Thin Solid Films*, 2010, **518**, p 1851-1878
15. W. Garkas, C. Leyens, and A.F. Renteria, Sythesis and Characterization of Ti_2AlC and Ti_2AlN MAX Phase Coatings Manufactured in an Industrial-Size Coater, *Adv. Mater. Res.*, 2019, **89-91**, p 208-213
16. J. Frodelius, M. Sonestedt, S. Björklund, J.-P. Palmquist, K. Stiller, H. Högberg, and L. Hultman, Ti_2AlC Coatings Deposited by High Velocity Oxy-Fuel Spraying, *Surf. Coat. Technol.*, 2008, **202**(24), p 5976-5981
17. J. Jiang, A. Fasth, P. Nylén, and W.B. Choi, Microindentation and Inverse Analysis to Characterize Elastic-Plastic Properties for Thermal Sprayed Ti_2AlC and NiCoCrAlY, *J. Therm. Spray Technol.*, 2009, **18**(2), p 194-200
18. M. Sonestedt, J. Frodelius, J.P. Palmquist, H. Högberg, L. Hultman, and K. Stiller, Microstructure of High Velocity Oxy-Fuel Sprayed Ti2AlC Coatings, *J. Mater. Sci.*, 2010, **45**, p 2760-2769
19. R. Trache, R. Puschmann, C. Leyens, L.-M. Berger, B. Matthey, and M. Herrmann, Thermally Sprayed Ti_3SiC_2 and Ti_2AlC MAX-Phase Coatings, in *Thermal Spray 2013: Proceedings of the International Thermal Spray Conference*, R.S. Lima, A. Agarwal, M.M. Hyland, Y.-C. Lau, G. Mauer, A. McDonald, F.-L. Toma, Ed., May 13-15, 2013 (Busan, South Korea), ASM International, 2014, p 74-78
20. N. Markocsan, D. Manitsas, J. Jiang, and S. Björklund, MAX-Phase Coatings Produced by Thermal Spraying, *J. Superhard Mater.*, 2017, **39**(5), p 355-364
21. H. Assadi, H. Kreye, F. Gärtner, and T. Klassen, Cold Spraying: A Materials Perspective, *Acta Mater.*, 2016, **116**, p 382-407
22. J.-O. Kliemann, H. Gutzmann, F. Gärtner, H. Hübner, C. Borchers, and T. Klassen, Formation of Cold-Sprayed Ceramic Titanium Dioxide Layers on Metal Surfaces, *J. Therm. Spray Technol.*, 2010, **20**(1-2), p 292-298

23. H. Gutzmann, F. Gärtner, D. Höche, C. Blawert, and T. Klassen, Cold Spraying of Ti_2AlC MAX-Phase Coatings, *J. Therm. Spray Technol.*, 2013, **22**, p 406-412
24. B.R. Maier, B.L. Garcia-Diaz, B. Hauch, L.C. Olson, R.L. Sindelar, and K. Sridharan, Cold Spray Deposition of Ti_2AlC Coatings for Improved Nuclear Fuel Cladding, *J. Nucl. Phys. Mater. Sci. Radiat. Appl.*, 2015, **466**, p 1-6
25. T. Go, Y.J. Sohn, G. Mauer, R. Vaßen, and J. Gonzalez-Julian, Cold Spray Deposition of Cr_2AlC MAX Phase for Coatings and Bond-Coat Layers, *J. E. Ceram. Soc.*, 2019, **39**, p 860-867
26. M.A. Piechowiak, J. Henon, O. Durand-Panteix, G. Etchegoyen, V. Coudert, P. Marchet, and F. Rossignol, Growth of Dense Ti_3SiC_2 MAX Phase Films Elaborated at Room Temperature by Aerosol Deposition Method, *J. Eur. Soc.*, 2014, **34**, p 1063-1072
27. J. Henon, M.A. Piechowiak, O. Durand-Panteix, G. Etchegoyen, Dublanche-Tixier, C. Dublanche-Ticier, P. Marchet, B. Lucas, and F. Rossignol, Dense and Highly Textured Coatings Obtained by Aerosol Deposition Method from Ti_3SiC_2 Powder: Comparison to a Dense Material Sintered by Spark Plasma Sintering, *J. Eur. Soc.*, 2015, **35**, p 1179-1189
28. M.W. Barsoum and M. Radovic, Elastic and Mechanical Properties of the MAX Phases, *Annu. Rev. Mater. Res.*, 2011, **41**, p 195-227
29. M.W. Barsoum, *MAX Phases Properties of Machinable Ternary Carbides and Nitrides*, 1st ed., Wiley, Hoboken, 2013
30. M. Sokol, S. Kalabukhov, E. Zaretsky, and M.W. Barsoum, Abnormal Response of Ti_3SiC_2 to High Strain-Rate Loading, *Phys. Rev. Mater.*, 2019, **3**(6), p 063010
31. M.W. Barsoum, T. El-Raghy, C.J. Rawn, W.D. Porter, H. Wang, E.A. Payzant, and C.R. Hubbard, Thermal Properties of Ti_3SiC_2, *J. Phys. Chem. Solids*, 1999, **60**, p 429-439
32. H. Warlimont, Ceramics, *Springer Handbook of Condensed Matter and Materials Data*, W. Martienssen and H. Warlimont, Ed., Springer, Berlin, 2005, p 460-461
33. I.M. Hutchings, *Tribology: Friction and Wear of Engineering Materials*, 1st ed., Butterworth-Heinemann, London, 1992
34. T. El-Raghy, A. Zavaliangos, M.W. Barsoum, and S.R. Kalidindi, Damage Mechanisms around Hardness Indentations in Ti_3SiC_2, *J. Am. Ceram. Soc.*, 2005, **80**(2), p 513-516
35. M.W. Barsoum, D. Brodkin, and T. El-Raghy, Layered machinable ceramics for High Temperature Applications, *Scripta Mater.*, 1997, **36**(5), p 535-541
36. F. Zhang, S. Yan, C. Li, Y. Ding, J. He, and F. Yin, Synthesis and Characterization of MAX Phase Cr_2AlC Based Composite Coatings by Plasma Spraying and Post Annealing, *J. Eur. Ceram. Soc.*, 2019, **39**(16), p 5132-5139
37. J. Singh, M.F. Wani, S. Banday, C. Shekhar, and G. Singh, Nano Scratch and Nanoindentation: An Approach to Understand the Tribological Behavior of MAX Phase Material Ti_2AlC, *IOP Conf. Ser. Mater. Sci. Eng.*, 2019, **561**, p 012111